TALLINN UNIVERSITY OF TECHNOLOGY
School of Information Technologies

Rauno Jõemaa 163556 IVEM

DEVELOPMENT OF AN ARTIFICIAL NEURON IN A MICROFLUIDIC CHIP

Master's thesis

Supervisor: Tamás Pardy
PhD

Tallinn 2018

TALLINNA TEHNIKAÜLIKOOL
Infotehnoloogia teaduskond

Rauno Jõemaa 163556 IVEM

TEHISNEURONI ARENDUS MIKROVEDELIK-KIIBIS

Magistritöö

Juhendaja: Tamás Pardy
PhD

Tallinn 2018

Author’s declaration of originality

I hereby certify that I am the sole author of this thesis. All the used materials, references to the literature and the work of others have been referred to. This thesis has not been presented for examination anywhere else.

Author: Rauno Jõemaa

12.05.2018

Abstract

Artificial neurons have been a scientific puzzle since the year 1943. The first artificial neurons being done with electronics, puts into perspective the development priorities of human technology. Only in the most recent decades has the concept of mimicking neurons biologically risen into the spotlight to compete with the slow progress of neuromorphic computing. The surfacing biomimetic projects with human cells have found a solid footing in the field of microfluidics. A microfluidic artificial neuron could provide further insight into the central nervous systems of humans and other animals. Aside from pursuing to find the root of human cognition or artificial intelligence, a shared medical condition could be a better target. It is estimated that globally, about 50 million people are presently suffering from incurable brain diseases. The most common being dementia, having the total sum of treatments and relief medicine yearly cost close to a trillion Euros. The discussed technology, when further developed, could promise revolutionary knowledge about different brain disorders and how to permanently treat them.

This thesis will tackle the basic concepts of an artificial neuron using the fundamentals provided by previous research into action potentials by physiologists A. L. Hodgkin and A. F. Huxley and into the microfluidic artificial neuron concept by T. Levi and T. Fujii. The designs devised in this work are required to pass Finite Element Analysis. Successfully passed designs will be fabricated using 3D printing. For the assembly and experimental processes, off-the-shelf materials and microfluidics equipment will be used. The outcome of this thesis is an overview of the design development, simulation and testing process of an artificial neuron made in a microfluidic system.

This thesis is written in English and is 69 pages long, including 5 chapters, 59 figures and 18 tables.

Annotatsioon

Tehisneuroni arendus mikrovedelik-kiibis

Tehnisneuronid on püsinud teadusliku mõistatusena juba aastast 1943. Senise inimtehnoloogia arengu prioriteetid panevad perspektiivi esimesed tehisneuronid, mis olid tehtud elektroonika põhjal. Alles viimaste kümnendite jooksul on esile tõusnud bioloogiliselt neuronite jäljendamine ning asunud konkureerima neuromorfse arvutustehnoloogia aeglase edenemisega. Esile kerkinud inimese rakkudega seotud biomimeetika projektid, on leidnud kindla jaluse mikrovedelikunduse alast. Mikrovedelik tehisneuron võib anda teravama pilgu inimese ja muude loomade kesknärvisüsteemi. Jättes siiski kõrvale inimese tunnetuse allika ja tehisintellekti järele pürgimise, võiks sobivamaks sihtmärgiks olla ühendav meditsiiniline seisund. On hinnatud, et ülemaailmselt on ligikaudu 50 miljonit inimest, kes kannatatavad ravimatute ajuhaiguste käes. Enamlevinud on dementsus, millel ulatub summaarne ravi ja leevendus rohtude igaaastane kulu ligilähedale triljonile eurole. Edendades aruteldavat tehnoloogiat edasi on lootus jõuda murranguliste teadmisteni erinevate ajuhaiguste kohta ning kuidas neid lõplikult ravida.

Käesolev dissertatsioon võtab ette kõige põhilisemad tehisneuroni konseptsioonid fundamentaalsete aluste najal, mis on eelnevate uuringute tõttu saadavaks tehtud füsioloogide A.L. Hodgkin ja A.F.Huxley poolt ning mikrovedelik tehisneuroni konseptsioonid, uuritud T. Levi ja T. Fujii poolt. Antud töös välja töötatud disainid peavad läbima Lõplike Elementide Analüüsi. Edukalt läbinud disainid valmistatakse 3D printimisega. Koostamis ja eksperimenteerimis protsesside puhul kasutatakse saadavalolevaid kommertskomponente ja mikrovedelikundus tehnikat. Töö tulemuseks on ülevaade mikrovedelik tehisneuroni disaini arendamise, simuleerimise ja testimise protsessidest.

Lõputöö on kirjutatud inglise keeles ning sisaldab teksti 69 leheküljel, 5 peatükki, 59 joonist, 18 tabelit.

List of abbreviations and terms

AP	Action potential
TUT	Tallinn University of Technology
D1	Design 1
D2	Design 2
FEM	Finite Element Modelling
FEA	Finite Element Analysis
CAD	Computer-aided design
RT	Room temperature
LiBr	Lithium Bromide
NaCl	Sodium Chloride
STL	Stereolithography
CSV	Comma separated values
PTFE	Polytetrafluoroethylene
DC	Direct current
GL45	Standard laboratory bottle thread size

Table of contents

List of figures

List of tables

1 Introduction

Having self-awareness has enabled us to wonder about our existence and the ability to ask questions about it for a long time. This sense of wonder has been accompanied by a growing frustration, because we are still asking the same questions, at least philosophically speaking. Through scientific and medical research, enough knowledge has been accumulated to say that our thoughts and actions originate from our brains and that in average, the central nervous system of a human consist of approximately 86 billion neurons [1]. In comparison, we can count to twenty using our fingers and toes, 206 using our bones and into thousands if we have the tenacity, but to study a system whose element count reaches into billions and magnitude of connections even further, is rather difficult to comprehend. This is the present state of reality. The lack of deeper knowledge of our brains, has elevated the global healthcare costs into hundreds of billions of euros annually, just to provide relief to people with brain disorders [2]. This is an excellent example to emphasise the problems at hand. In addition, there are no treatments available for brain disorders like Parkinson's, Alzheimer's or Huntington's disease just to name a few. None of the named diseases are as rare as one would assume. Different forms of dementia, including Alzheimer's, are currently affecting people globally at a rate of 1 out of 150. This is unfortunately predicted to increase to 1 out of every 115 people by the year 2030 and 1 out of 75 by 2050 [3]. The increasing life span does not promote a peace of mind given that the aforementioned diseases could already be showing symptoms at ages between 50 and 70, that is with leaving out the possible early onset cases. The named diseases do not come only with mental hindrances but also a noticeable mortality rate, which has been kept relatively low with extensive relief treatments. Thanks to global associations such as Alzheimer's Disease International (ADI), the rapid spreading of global awareness about these facts is providing a strong motivation for research into finding solutions and an increasing number of sources for funding.

Research into treatments of brain disorders currently relies on animal trials. Insufficient understanding of the human brain binds us from conducting human trials safely or with even a small degree of confidence. This shortcoming has been a thorn in the side of the

scientific community for decades. But thanks to the ever-advancing computational proficiency, there is a good number of relevant ongoing projects such as the digital reconstruction of the brain – Blue Brain (CH), brain-related research infrastructure based on exascale supercomputers – Human Brain Project (EU), brain mapping – Brain/MINDS (JP), funding and supporting of the development of innovative technologies for brain research – BRAIN Initiative (US) and research into the basis of cognition – China Brain Project (CN). Besides the funding perspective, all mentioned projects strive towards the replication of the brain or one of its core functions. Replication or mimicry of anything biological would require an excellent grasp of the fundamentals. However, even with it, biomimetics is a difficult methodology. Nature's complex structures and microscopic systems optimised for liquid organic environments often tend to favour electrochemistry. A good illustration of this would be to look at a nerve cell in the brain. The diameter of the channel along which neurons propagate electrical signals resides typically around 1 micrometer which is a millionth of a meter [4]. Moreover, this channel is covered with many small valve-like structures with cross-sections of about 50 atoms in length, which broadly interprets into 50 Angstroms or 5 nanometers. For comparison, the smallest transistor gate length demonstrated so far, has reached the 5 nanometer range, but it is expected that this technology would not be commercially available before the year 2020 [5]. Furthermore, it is important to note that a transistor consists of functional parts of an amount which could be counted on the fingers of a single hand. It has a much simpler structure and it does not work well with organic ions or liquids. To make this more relevant, it becomes rather apparent, that a different technology entirely, might be a more suitable option when trying to develop an artificial neuron for medical and general cognition research.

A promising alternative could be found in microfluidics, which is a developing new technology that utilises fluid control within channelled structures with dimensions below 1 millimeter. The defining features of such devices include low reagent consumption, low cost, faster results and the effects of laminar flow which can be used gain precision control over the mixing of different ionic concentrations. Slow physical processes such as molecular diffusion through porous membranes can be magnified with low liquid volumes and relatively large surface areas of porous membranes. This makes it a very attractive methodology for biomimicry. However, adopting this technology is challenging, because the foundation for developing a microfluidic chip for research is in

its infancy and rather expensive for newcomers. As electronics grew together with propelling ideas such communication, radio, television, computers etc., development in microfluidics is driven mostly by a narrow slice of the research community. The careful growth of microfluidics is guided mainly by medical research. The fields popularization is rather slow due to the lack of immediate applications. Regardless, it does however, provide an attractive set of advantages for being the optimal alternative to common electronics in biomimetics (see Table 1).

Table 1. Comparison between microfluidics and electronics in biomimetics

	Microfluidics	**Electronics**
Cost	Lower	Higher
Liquid handling	Optimal	Very poor
System type	Analog system (fluid physics, ion concentrations)	Digital system (limited by bit resolutions)
Compatibility with living tissues and organic ions	Chemically inert structural materials	Corrosion, short circuiting, thermal runaway
Minimum control speeds	Adequate (milliseconds)	Very fast (nanoseconds)
Interface	Fluidic/hybrid	Purely electrochemical

Even by not offering an advantage in control speeds, there is enough favourability towards microfluidics. Regarding the slower control speeds, functions in biological organisms tend to change at the millisecond scales as well. Microfluidics is better when pursuing the replication of nature's organic functions. Closely replicating familiar organic systems, as is done with the technology of Organ-on-a-chip (OOC), research related to brain tissues has become more popular. By using microfluidics, it is now possible to imagine a wide range of approaches when doing R&D on the topics such as neurons in vitro and artificial neurons in microfluidic chips [6]. The latter, while being the more novel of the two, has an obvious lack of related research materials. The scarcity of new articles in this field, makes it an excellent time to join the endeavour.

This paper was made as a result of documenting the pursuit of widening the knowledge about artificial neurons in microfluidics. It contains research about the fundamentals of the biological and artificial neuron, its compatibility and feasibility with off-the-shelf

microfluidics tools in conjunction with customized methodologies, ultimately leading to one specific development process of an artificial neuron. The foundation of this thesis is split into 3 parts; novelty and theory, covering the characteristics of action potentials and the artificial neuron development principles; materials and methods, covering the proof-of-concepts through simulations and experiments; results and discussion, where both simulation and experiment results are covered and analysed.

2 Theoretical Background

As was previously stated, the brain in its entirety is not a feasible target for biomimicry. A more sensible option would be the brain's smaller fundamental component – the neuron. A neuron is a biological cell that can be defined by its two unique functions. One of which is to act as a propagation path for information, the other is best described with an analogy of sōzu: as the propagating information within living organisms have different meanings and weights of relevance, the neuron requires a certain amount of specific stimulus to generate a signal, much like the bamboo fountain eventually pivots and quickly empties after being filled by a comparably smaller stream of water. The generated signal is called the action potential (AP). After an action potential crosses the neuron, it either continues propagating along another neuron or leads to an end event in the organism – movement, feeling or a stream of familiar senses (e.g. hearing a word – thought). The action potential is not a unit of information without the combined complex weighted path it takes. Regardless of being called a unit, the information is always unique and a complex mathematical process. Due to time and resource constraints, this thesis however, omits the rules of weighing the external stimuli and narrows down its focus to the realisation of the action potential.

2.1 Action Potential

The discovery of electrical impulses in nerves discovered on 1843 by Emil du Bois-Reymond, the action potential as it is known today was first seen by Alan Lloyd Hodgkin and Andrew Fielding Huxley in 1939 [7], [8]. By now, the most recognisable biological representation of an action potential is shown on Figure 1 (Page 16).

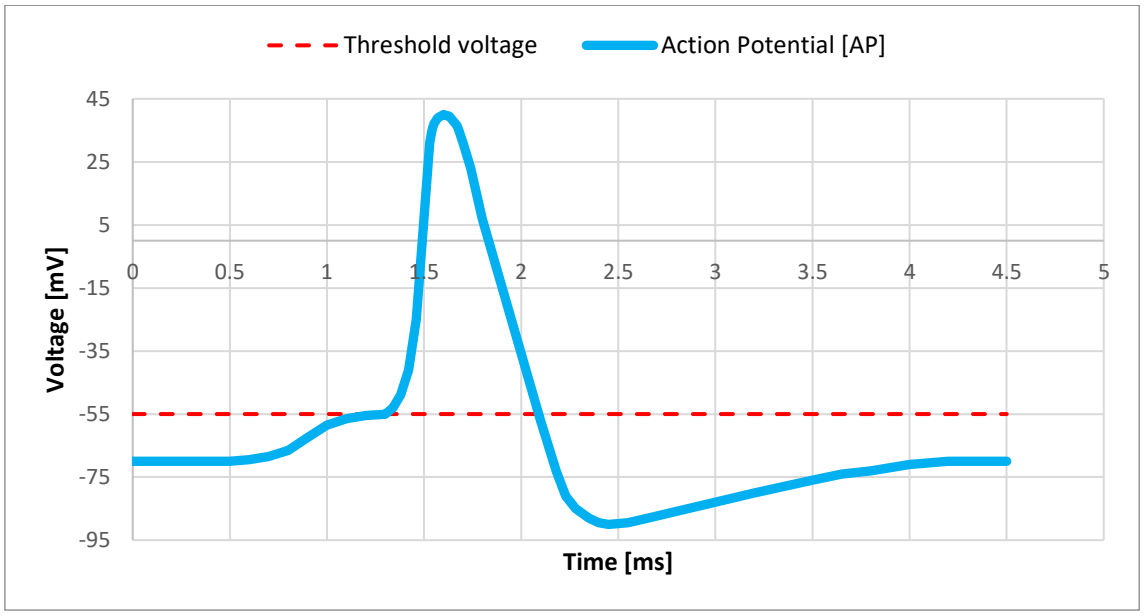

Figure 1. Action potential – voltage vs. time graph

This paragraph about action potentials is segmented into two parts which will detail the biological AP example shown on Figure 1 and the reproduction of it by relying on the logic used by artificial biomimetics.

2.1.1 Biological AP

A biological neuron can be split into three major parts aside from its normal cell nucleus and soma: dendrites, axon and axon terminals. By using dendrites and axon terminals a neuron can connect with other cells and share information through synapses. Every neuron has one unidirectional signalling path which is called the axon. The axon determines the form of the signal, regulates the firing rate and increases the distance the information can travel. The signal or rather a pulse is an interpretation of a moving localised voltage potential. This voltage potential is defined by the differences between the ionic concentrations within and around the neuron [9]. The normal ionic concentration within a neuron makes it negatively charged compared to the outside concentration. In its normal state a.k.a. resting state, the neuron is polarized to about -70 mV. For being able to hold the neuron polarised and to be able to generate an AP, neuron specific membrane proteins need an introduction. A minimum of three types of membrane proteins are required for the aforementioned functions, all of which act like valves to regulate the ionic concentrations. Two of these proteins are voltage-sensitive and tend to open in waves along the axon, while others are active continuously, trying to keep the neuron at its resting state. To generate an action potential, the neuron must receive an external stimulus

which would bring the intracellular ionic concentration to a threshold voltage of about -55 mV as is shown on Figure 2.

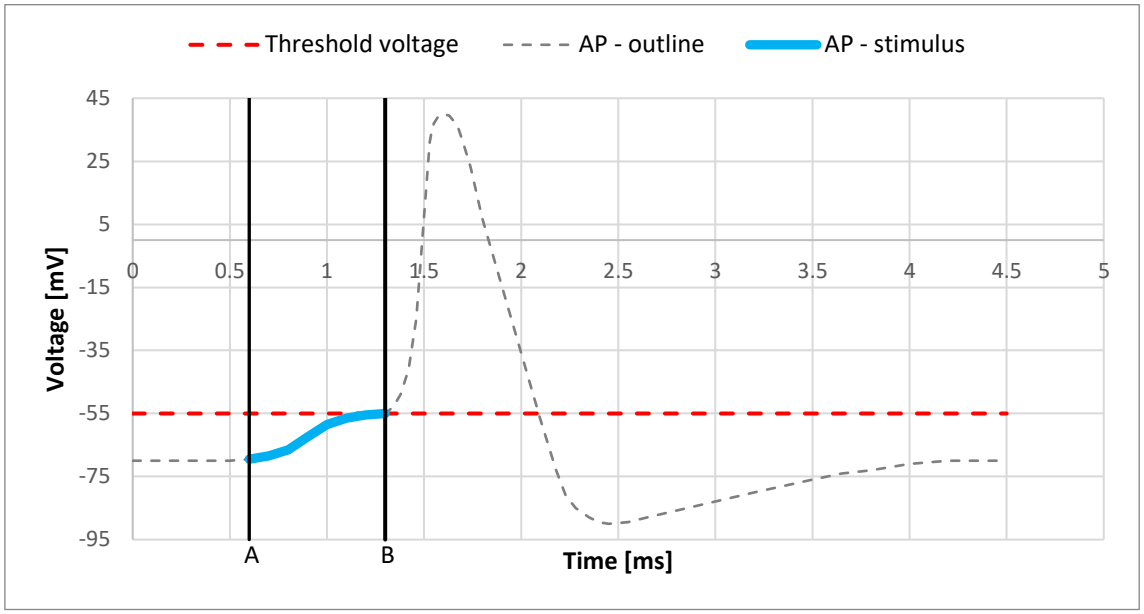

Figure 2. AP stimulus segment – voltage vs. time graph

After crossing the threshold voltage, like the domino effect, one type of voltage-sensitive valves would open one by one down the axon. This process, otherwise known as depolarisation, would produce a voltage reversal over the neuron's membrane until the gradient reaches about 40 mV (Figure 3).

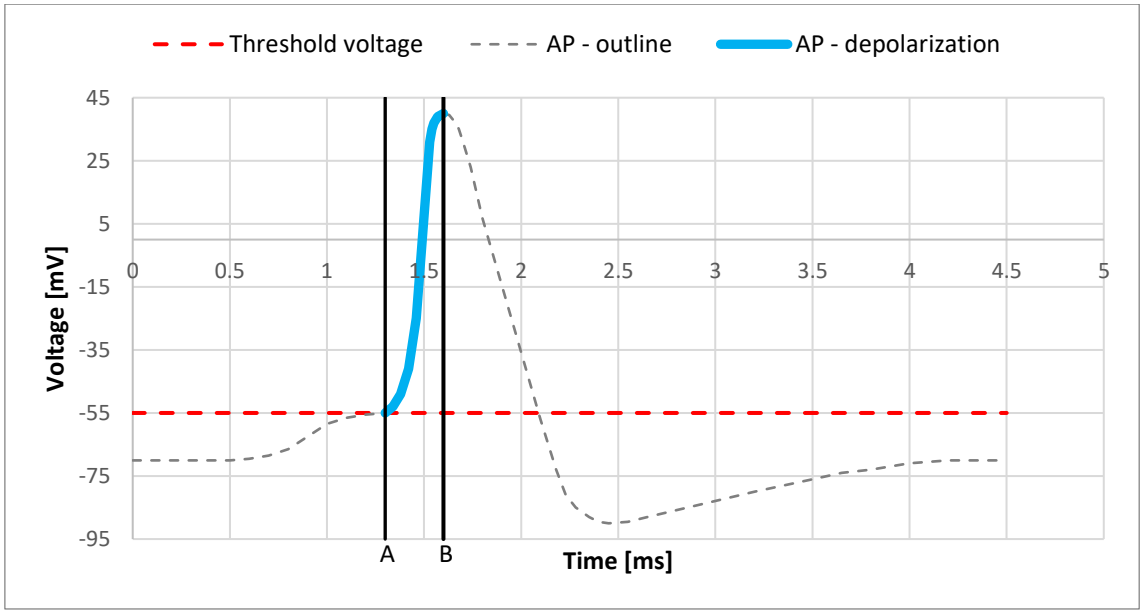

Figure 3. AP depolarization segment – voltage vs. time graph

The depolarisation voltage is limited by a secondary threshold defined by both of the voltage-sensitive proteins. Shortly after reaching this depolarisation limit, a second wave

of valves would open and generate the falling edge of the pulse while accompanied by closing of the first valves (Figure 4).

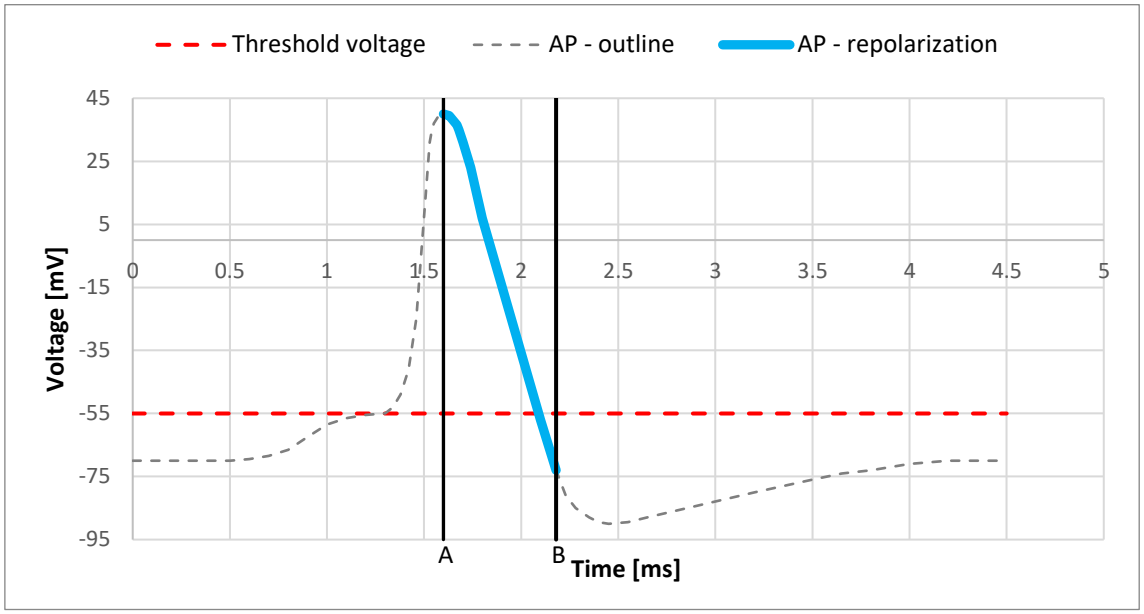

Figure 4. AP repolarization segment – voltage vs. time graph

This process is known as repolarisation. The second set of voltage sensitive valves are more slow-acting and because of this, the neuron's internal concentration would become more negative than its initial resting state and this is known as the hyperpolarisation effect (Figure 5).

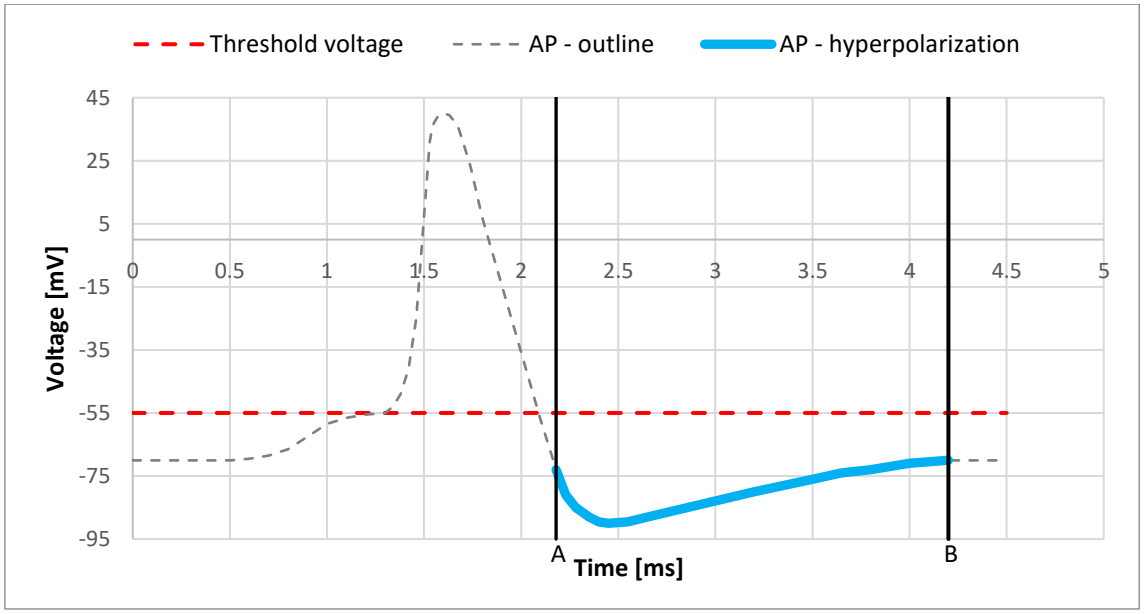

Figure 5. AP hyperpolarization segment – voltage vs. time graph

Even so, the second type valves will eventually close at about -90 mV and the lesser effects of the continuously active valves will take over as they would gradually return the

neuron to its resting state. This way, the ionic concentrations within the neuron would return to normal and it would be possible to generate another pulse. This final stage is called the refractory period. This concludes the overview of the biological action potential.

2.1.2 Artificial AP

When artificial action potentials become the target of discussion, the fundamentals will most often lead back to the efforts made by A. L. Hodgkin and A. F. Huxley in the 1950s [10]. By using the Nernst equation (1), they were able to calculate the equilibrium potential of different ionic concentrations across a membrane at any given time [9].

$$E_0 = \frac{RT}{zF} \ln \frac{C_o}{C_i} \tag{1}$$

Hodgkin and Huxley made thorough calculations for both main organic ions involved in the biological AP generation and leakages – Na and K, but as demonstrated by T. Levi and T. Fujii, the use of only one element is enough to begin generating AP-like shapes [6], [10]. This meant that the simulation and experimental processes could be made faster for proving design concepts. To reduce computational space even further, a microfluidic chip design for generating action potential could be proven by just simulating AP specific voltage levels as explained with Figure 6.

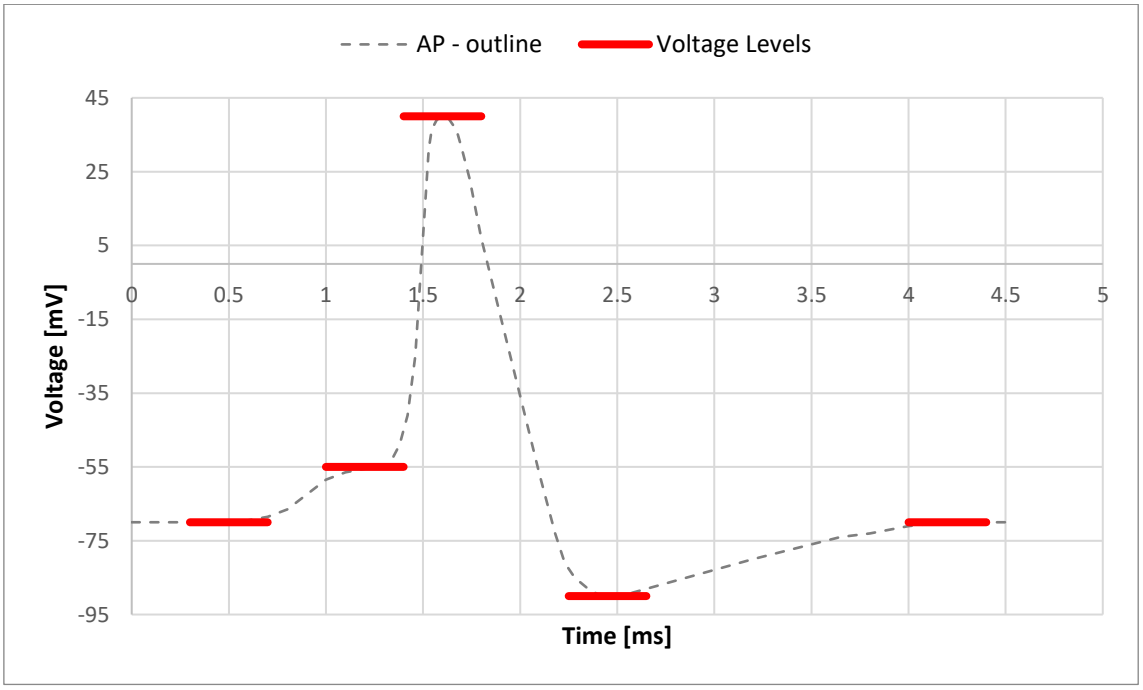

Figure 6. AP characteristic voltage levels

If the conceived design can acquire voltage levels of the resting state (-70 mV), threshold level (-55 mV), typical depolarization (40 mV) and hyperpolarization levels (-90 mV), further development becomes feasible. To simulate action potentials with fluidics and chemical concentrations over time, the use of FEM software would become a necessity. Since simulators such as COMSOL are purposefully generic for many scientific fields, integrating the Nernst equation (1) and its components into the simulator setup is required. The parameters of the Nernst equation at room temperature can be seen in Table 2.

Table 2. Definitions of Nernst equation parameters

Variable	**Description**	**Value**
R	Universal gas constant	$8.314\ J/(mol \cdot K)$
T	Temperature in Kelvins	$298.15\ K$
z	Valence of the ion	1
F	Faraday constant	$96485\ C/mol$
C_o	External concentration of the ion	$(value)\ mol/m^3$
C_i	Internal concentration of the ion	$(value)\ mol/m^3$

If after achieving the characteristic voltage levels, the entire AP shape is desired, for reference, a well proven HHsim simulator could be used (see Figure 7).

Figure 7. Hodgkin-Huxley AP simulator (HHsim); Three example action potentials

Only simulating voltage levels can be achieved by using stationary equations, excluding time derivations and reducing simulation times. On the other hand, by including the changing time variable, the computation load increases exponentially. However, this does

not need to be done on paper or by hand, since COMSOL enables the use of time dependent equations. For microfluidic simulations, physics modules such as Laminar Flow and Transport of Diluted Species ought to be used. By including the laminar flow physics, flow fields become incompressible, defining the material densities as constants throughout the flow streams. For calculating the reaction rate, COMSOL uses a time-dependent convection-diffusion equation (2).

$$R_i = \frac{\partial c_i}{\partial t} + \nabla \cdot (-D_i \nabla c_i) + u \cdot \nabla c_i \qquad (2)$$

The reaction rate of a species i is therefore equal to the summation of the concentration diffusion rate ($-D_i \nabla c_i$), convection ($u \cdot \nabla c_i$) and total concentration change in time ($\frac{\partial c_i}{\partial t}$).

With equation (2), COMSOL operates with the transport of liquids on a micro scale. Membrane potentials would be calculated from the Nernst equation (1) using the concentrations derived from equation (2). To create designs in efforts to simulate action potentials in COMSOL, mentioned equations alone, will not provide instructions on how to design the device geometrically.

2.2 State of the Art

The idea of an artificial neuron is common in electronics, but rare in microfluidics. The number of articles published related to neurons in microfluidics is low. So far, there are two that stand out, “Microfluidic Neurons, a New Way in Neuromorphic Engineering?” published by Timothée Levi and Teruo Fujii, in 2016 and “An organic electronic biomimetic neuron enables auto-regulated neuromodulation” published by Daniel T. Simon et al., in 2015 [6], [11]. The first is highly relevant to this work and is detailed in the following paragraphs.

The microfluidic artificial neuron by T. Levi and T. Fujii was made using various microfluidic techniques and fabricated using off-the-shelf materials. They proposed a direct alternative to state-of-the-art silicon based artificial neurons. In summary, two separated reservoirs with controllable ion concentrations were used. Reservoirs were connected to channels that were separated by a Nafion membrane through which only cations could permeate. The Nafion membrane was further split from the ion reservoirs by Quake valves (Figure 8, Page 22).

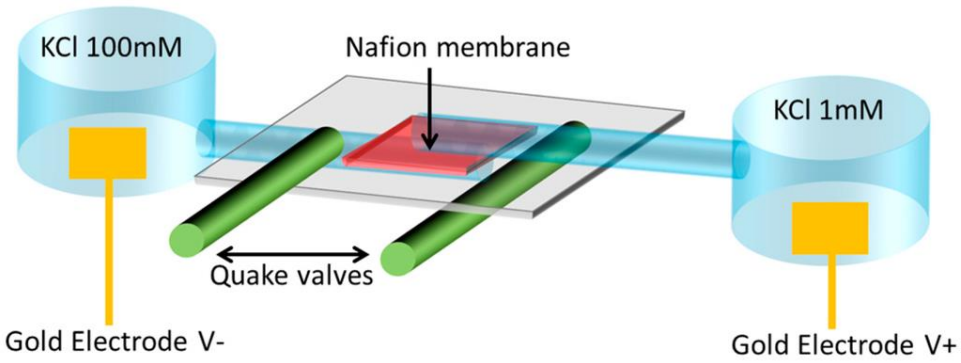

Figure 8. State-of-the-art diagram of an microfluidic artificial neuron device [6]

Quake valves enabled to control the opening and closing of the channel through the use of air pressure. The closed channel would ideally stop the concentration flow and remove the connection between reservoirs. This process would cause the measured voltage between the gold electrodes to fall to zero. However, this was not the case due to the limitations of the Quake valve. The consequent results obtained from T. Levi and T. Fujii can be seen on Figure 9.

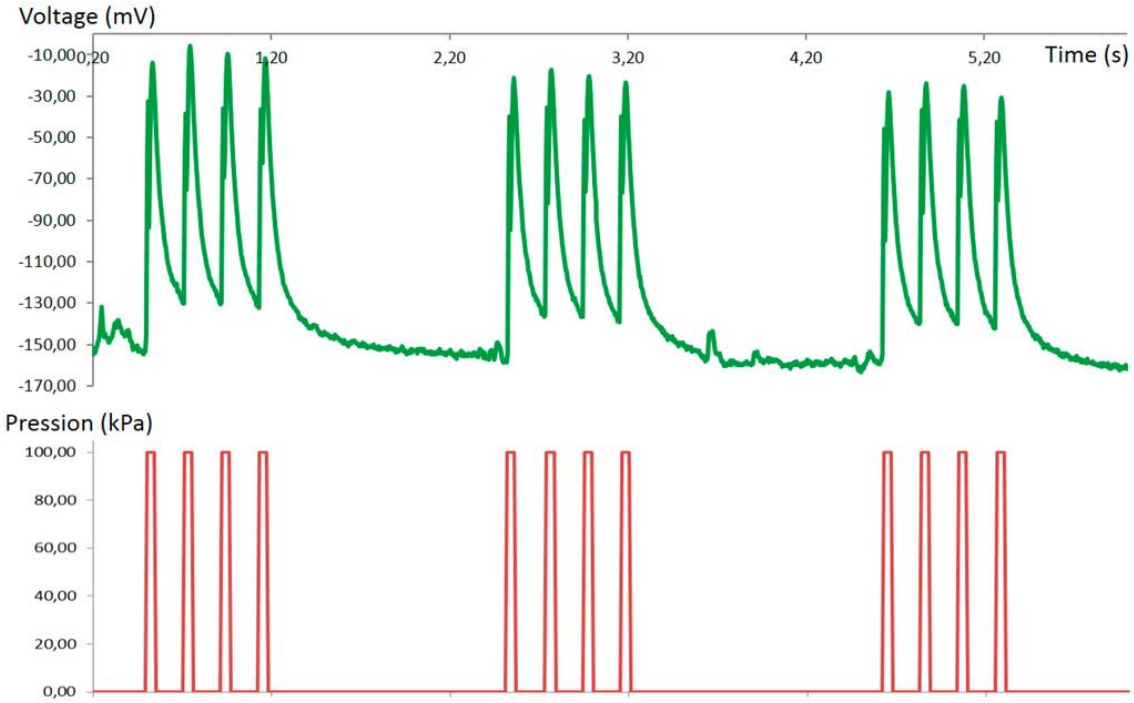

Figure 9. Artificially generated action potentials in a microfluidic device [6]

Voltages graphed on Figure 9, show that the proposed artificial neuron design did not provide enough functionality to produce positive voltages. More importantly however, the repeatability of the action potentials is noteworthy.

The electronic/organic hybrid artificial neuron developed by Daniel T. Simon et al. documented in the "An organic electronic biomimetic neuron enables auto-regulated neuromodulation", was made to propose a design of an artificial neuron device and demonstrate the feasibility of neuronal signaling prosthetics [11]. They managed to design and build a device which could transform chemical energy into electrical from one end and in a reversal in the other end, thus mimicking the synapses across a biological neuron (see Figure 10).

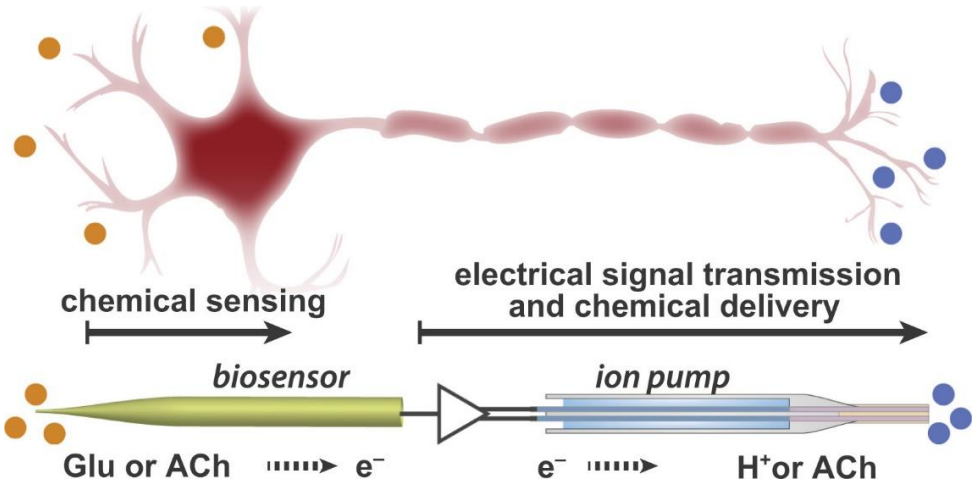

Figure 10. State-of-the-art diagram of an electronic/organic artificial neuron [11]

The device depicted on Figure 10 was built with an off-the-shelf amperometric highly selective ion sensors to detect neurotransmitters such as acetylcholine (ACh) or glutamate (Glu) on one end of the device (biosensor) [11]. This ion sensor could transduce specific ionic concentrations into current (about 1 nA / 10 µM @ > 20 µM). This process however, was very slow and required the voltage supply of about 500 mV by external means. In the middle of the device was hardware/software programmable chip, which played the role of the axon hillock [11]. The other end of the device (ion pump) was a reservoir filled with neurotransmitters (H^+ or ACh) enclosed by a thin membrane on the tip. When enough neurotransmitters were detected at the biosensor and the defined threshold value was crossed, the organic electronic ion pump (OEIP) started to release neurotransmitters from the other side of the device, acting as the biological axon terminal. OEIP can be very precise (1 ion per electron) [11]. The results of excitation level testing obtained by Daniel T. Simon can be seen on Figure 11 (Page 24).

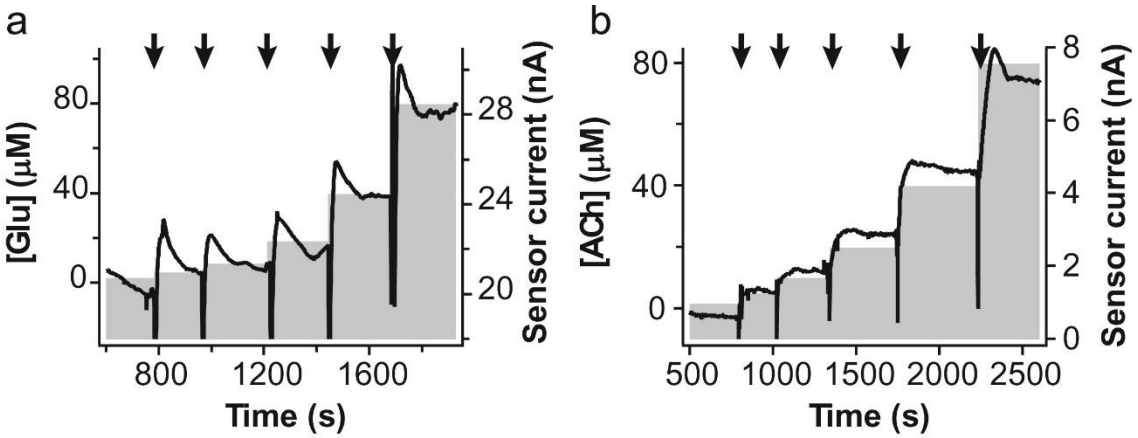

Figure 11. Continuous current levels were generated by adding different amounts of neurotransmitter (Glu and ACh) concentrations [11]

Aside from the validation methodology, electronic/organic hybrid device proposed by Daniel T. Simon et al., does not offer directly integrable design principles for this thesis. The two articles described, provide a solid foundation to start the development of our artificial microfluidic neuron.

2.3 Design Theory

In this thesis, the simplicity of designs is sought for the chance to save time and resources. Besides efficiency, it is easier to analyse fewer variables. Considering the natural intra- and extracellular environments of a neuron, two channels, an ion selective membrane and a valve as proposed by T. Levi and T. Fujii, are the minimum requirement. However, it is a difficult task to incorporate a controllable valve inside a microfluidic chip. As was the case on the system shown on Figure 8 (Page 22), PDMS and Quake valves did not work together. The pressure limit measured was 200 kPa while higher values caused the chip to break [6]. If PDMS were to be used at all, a different valve or chip design would prove essential. Besides the concepts of typical valves, by having control over the channel flows themselves could be viewed as valve-like effects. By controlling fluid flows within a design, control over the mixing rates of ionic concentrations can be obtained as well. This in turn could enable the generation of more stable AP signals over a broader range of voltage levels. Since controlled exchange of ionic concentrations over a membrane is required for AP generation, high mixing and coverage of the concentration in the opposite medium is beneficial. At microscales laminar flow takes over and diffusion mixing is favoured. Thus, by adding interfacial areas such as bends and curves to the microfluidic designs, mixing rate could be increased.

3 Materials & Methods

There are various approaches that could be taken to develop a microfluidic artificial neuron. From an economic perspective, before experiments, the proposed designs are first required to be proven feasible. To grasp the available experimental options with microfluidic devices and narrow down the selection, this paragraph is segmented into four parts, starting from the proof-of-concept. Next two steps include the evaluation of prototyping options and structural materials respectively. Last one being the experimental setup, including systemic methods, fabrication, assembly, equipment and measurement methods.

3.1 Proof-of-Concept

The implementation of an artificial neuron in microfluidics can be complex and economically straining. To prove the feasibility and functional characteristics of various, comparable designs, simulations and modelling are required. FEA simulation and CAD modelling were performed iteratively to optimize the designs, as detailed in Section 3.1.1. The optimized device designs are presented in Section 3.1.2.

3.1.1 FEA Simulations

The following simulations were created by using the virtual environment of COMSOL Multiphysics® version 5.1. Simulations were made in two dimensions with parameters within the limitations of the available prototyping equipment. The number of calculable points, otherwise known as degrees of freedom (DOFs) in COMSOL, were kept low (less than 10 000) to reduce the convergence time (Mesh – Element size: coarse; coarser). This caused the average element quality to drop, but the ratio of radius remained above 0.8 (better is closer to 1). Because the designs made were simple, without largely varying feature sizes, the element deformations at element quality of 0.8 were acceptable.

Two design paths were proposed and pursued. Each one having a different approach on how to manipulate the ionic concentrations over the ion-selective porous membrane. This in turn would greatly affect the functionality and the limitations of the designs. The design advantages and disadvantages have been put together into Table 3 (Page 26).

Table 3. Comparison of designs

	Flow pressure control	**Cross-flow valve**
Advantages:	• Simple design • Easy assembly • Cheaper • 2 channels • Fast reaction speeds • Fast recovery speeds • Under- and overshoot capability	• Better control over the ionic concentrations • Longer lifetime • Easy to attain the resting state • Signal repeatability
Disadvantages:	• Difficult to accurately control the ionic concentrations • Shorter lifetime • Pressure is limited by the strength of the membrane • Difficult to attain the resting state • Signal repeatability requires compensating flow algorithms	• Difficult to assemble • 3 channels • Slow reaction speeds • Slow recovery speeds • Under- or overshoot effects require a more complex flow control signal

Design 1: Flow Pressure Control

Method: Controlling the differential pressure gradient across the porous ion-selective membrane to change the concentrations forcefully.

Description: The design includes two joined channels perpendicular or parallel to each other, separated by an ion-selective membrane. One of the channels represents the intracellular environment while the other channel represents the extracellular. When channels are filled with their respective solutions, the membrane is continuously conducting cations, trying to equalise the ionic concentrations between the environmental differences due to the electrochemical forces acting across the membrane. This is a relatively slow process when liquids are stationary. When the pressure within the intracellular channel were to be increased, the differential pressure across the membrane would induce a stronger flow through it. The created pressure difference could also cause bowing of the membrane, increasing its surface area which consequently would boost the flowrate through the membrane. Higher flowrates through the membrane would rapidly

balance the concentrations within the channels as well as cause a small overshoot, hence, causing a voltage reversal. The explained action would be called the “depolarisation” process. In contrast, when the pressure within the intracellular channel is halted and instead, increased within the extracellular channel, the ionic concentrations would quickly normalise. But due to the pressure difference over the membrane, some of the cations would pass over to the intracellular region, causing an undershoot. This feature is very suitable for achieving the desired action potential-like hyperpolarisation curve.

Design layout: One of the main reasons for making this design was to prove the concept of an artificial neuron within a microfluidic chip. The other reasons were to learn more about the behaviour of an ion-selective porous membrane and to test the simplest designs to attain artificial action potentials. The geometry of the design was scaled to the highest resolution the used prototyping equipment could provide. A low number of degrees of freedom and elements enabled more rapid simulations. For visualisation, the triangular and quadrilateral elements can be seen on the design 1 mesh view on Figure 12.

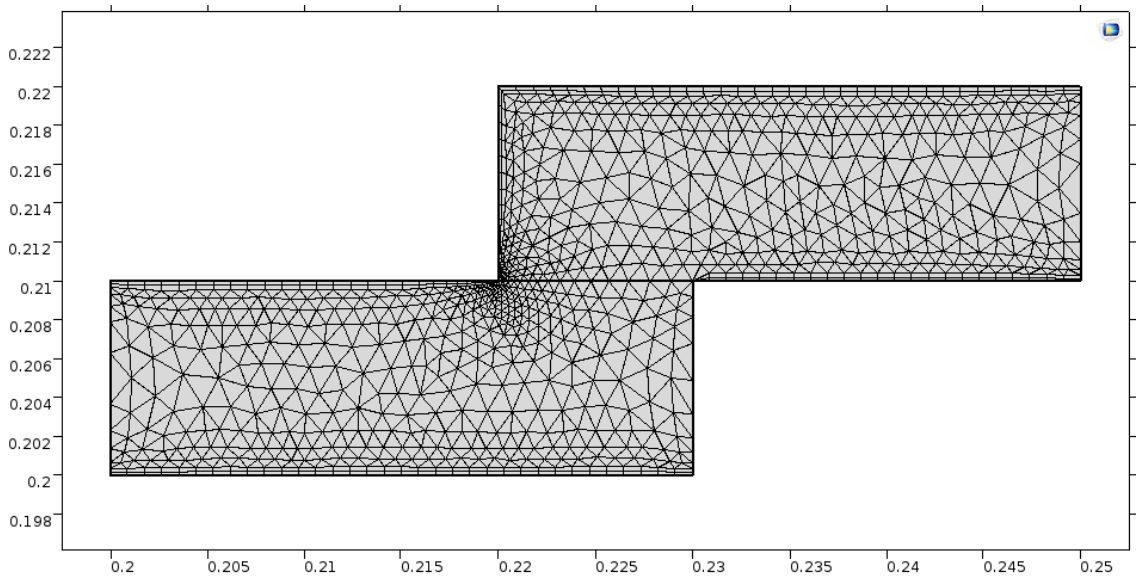

Figure 12. Mesh view of design 1 – parallel channels

Both axes of the mesh view are presented in millimetres. While the larger triangular elements have been organised to the central, more open regions of the channels, the smaller triangular and quadrilateral elements or polygons have populated the interfacing surfaces and corners. This is due to the use of laminar flow physics, where higher incident regions during liquid flow are located at the interface regions and the lowest changing regions remain in the middle of the channel where the flowlines are most true.

The mesh does not give much insight into the design functionality. It would seem as if there was just the one zig-zag channel, however, this is not the case. There are two channels, represented individually by top and bottom rectangles and even though the channel lengths are both equal, the system is asymmetric. This is due to having 3 open boundaries, 2 inlets and 1 outlet. Design 1 can be split into 3 separate critical parts, whose function and locations are shown on Figure 13,Figure 14 and Figure 15.

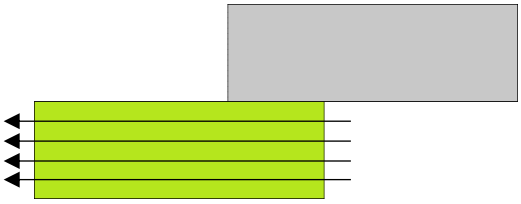

Figure 13. D1 - Extracellular channel/environment

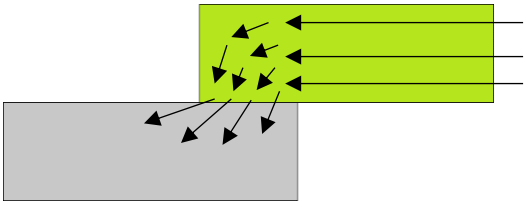

Figure 14. D1 - Intracellular channel/environment

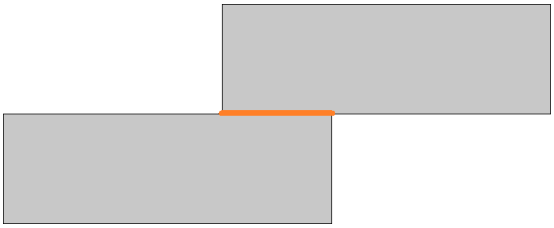

Figure 15. D1 - Ion-selective porous membrane location

To keep the incident regions at a minimum for the extracellular channel, shown on Figure 13, a straight channel geometry was optimal especially in laminar flow physics. In contrast, the intracellular channel (Figure 14) was specifically designed to be parallel with the extracellular to have the additional incident regions to induce faster mixing of the concentrations during inflow. The channel parameters are shown in Table 4.

Table 4. D1 geometric parameters in COMSOL

	Intracellular Channel [mm]	**Extracellular Channel [mm]**	**Channel Junction [mm]**
Width (x-axis)	0.03	0.03	0.01
Height (y-axis)	0.01	0.01	-

Simulation setup: Simulations were done using only water (H_2O) for the materials. Multiple material interactions would have required additional physics, which was not necessary for these simulations. By using only one element, different flows within separate channels could be distinguished by their ionic concentrations. Both the initial

and inflowing concentrations for both channels were derived from combined biological and artificial principles. The initial concentration in the intracellular channel was 140 mol/m^3 and 5 mol/m^3 for the extracellular. By keeping the concentration ratios relatively similar, the inflow concentration for the intracellular channel was 0.1 mol/m^3 and 0.01 mol/m^3 for the extracellular. These concentration amounts were enough, considering the parameters of the Nafion membrane simulated with. The thin diffusion barrier acting as the Nafion membrane, had a layer thickness of 1 μm and a diffusion coefficient ($D_{s,c}$) of 2.65E-10 m^2/s for positive ions [12]. For generating a minimum of 2 similar action potential signals, a simulation window of 30 ms was set. The suitable flow velocities for generating the action potentials within the given time were found through logical elimination. The used velocities are shown in the following Table 5 and Table 6.

Table 5. D1 extracellular normal inflow velocity control settings

Function Start [ms]	**Function End [ms]**	**Flow Velocity [m/s]**
0	5	0.06
5	6	-0.02
6	16	0.06
16	17	-0.02
17	30	0.06

Table 6. D1 intracellular normal inflow velocity control settings

Function Start [ms]	**Function End [ms]**	**Flow Velocity [m/s]**
0	5	0.00
5	6	0.04
6	16	0.00
16	17	0.04
17	30	0.00

Design 2: Cross-flow Valve

Method: Using a cross-flow channel between the intra- and extracellular environments, separated by ion-selective porous membrane(s) to function as a valve for diffusion rates.

Description: This design includes three channels parallel to each other, separated by ion-selective porous membrane(s). Cross-flow as the middle and intra- and extracellular environments as the side-channels. When all three channels would be filled with their

respective solutions and remain stationary, the porous membrane(s) would diffuse cations from the intracellular environment to the extracellular to bring the system concentrations into equilibrium. When measuring voltage over the cross-flow channel, a defined resting state voltage level is measured. By increasing the flowrate of the cross-flow, the electroconductive path would shrink, eventually cutting off the connection completely. By controlling the flowrates of all three channels, it is possible to generate the depolarisation as well as the repolarisation processes. It is only required to maintain the concentrations in both side-channels and stop the cross-flow to produce the repolarisation effect. Hyperpolarisation on the other hand would require adding additional complexity to the inflow signals. Methods such as channel flowrate reversal, utilising the overshooting effects by introducing rapid flowrate changes or altering the concentrations of the cross-flow solution could be implemented for achieving the desired results.

Design layout: Design 2 was made as a competitor to the first design and as an alternative to the one proposed by Timothée Levi and Teruo Fujii [6]. To address the pressure issue with quake valves, a channel blocking valve with an additional outlet is used, enabling us to relieve the pressure. Because the blocking material in this design is also a liquid solution, during its stationary stasis, ion flow can continue without any interface resistance as was the case with liquid-air interface [6]. The geometry (Figure 16) was designed to be symmetrical to keep the differential pressures across the membrane(s) as equal as possible and to avoid creating bottlenecks over the membrane(s).

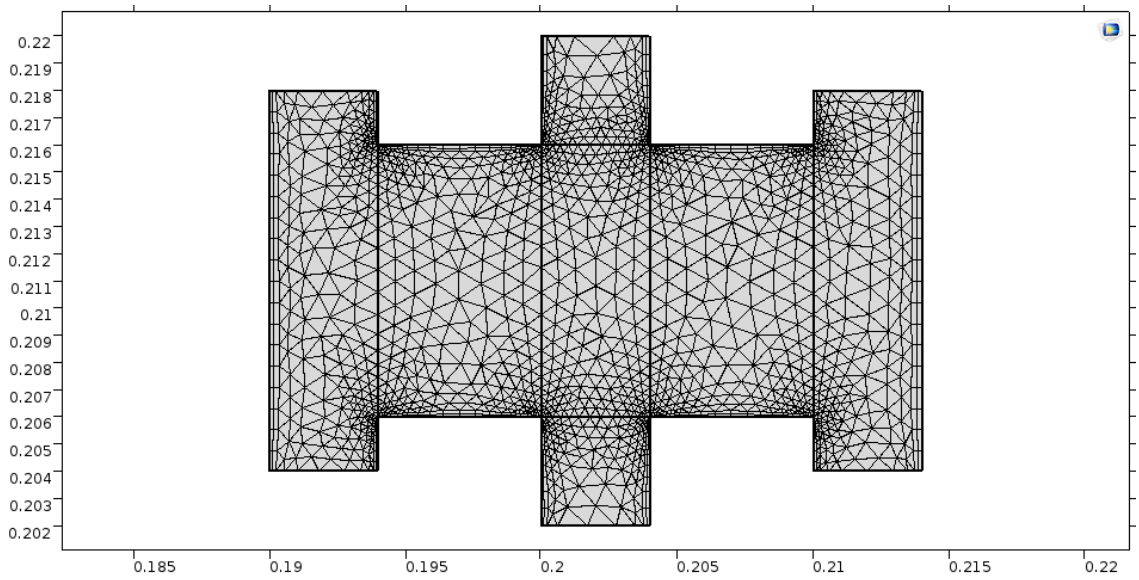

Figure 16. Mesh view of design 2

Both axes of the mesh view are given in millimetres, however, the sizes of geometric parts of the design within COMSOL are relative while choosing to use the physics of laminar flow. This gives the opportunity to run simulations using any desired geometric parameters and scale the model after the limitations the prototyping equipment might have. However, even if the physics of laminar flow were to remain stable over any scale, other components might not scale as well. For example, COMSOL is not able to calculate any physical effects on a diffusion layer (permeable membrane), which becomes more fragile as its surface area increases, causing a scenario where the simulation will not be able to predict the reality. Other important factors which are separate from laminar flow physics are the flowrates and the ionic concentrations. But these can be set to follow the geometry. In comparison to design 1, in design 2, every channel has its own inlet and outlet. All of the three channels are shown on Figure 17, Figure 18 and Figure 19.

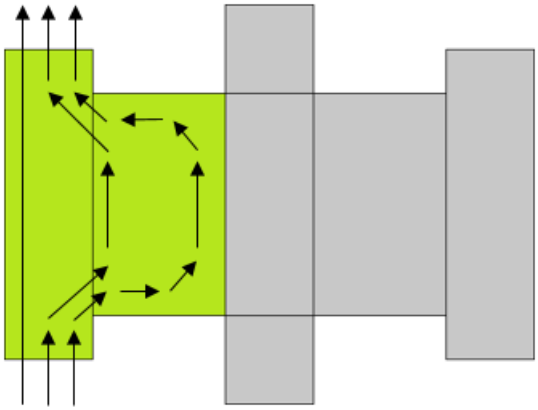

Figure 17. D2 - Extracellular channel/environment

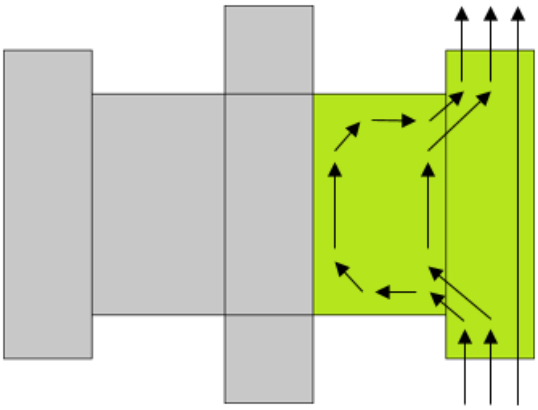

Figure 18. D2 – Intracellular channel/environment

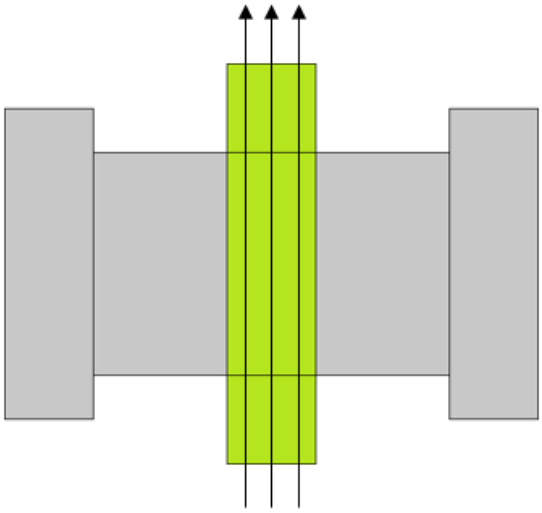

Figure 19. D2 - Cross-flow channel

As the motivation for this design stem from the design proposed by Timothée Levi and Teruo Fujii (Figure 8, Page 22), it started off with only one membrane, separating the extracellular environment from the rest (Figure 20).

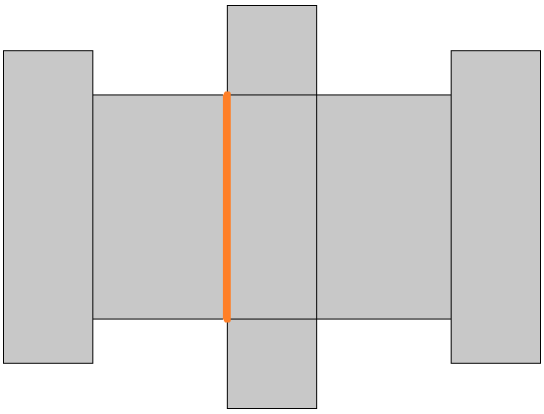

Figure 20. D2 - Ion-selective membrane between the extracellular and cross-flow channels

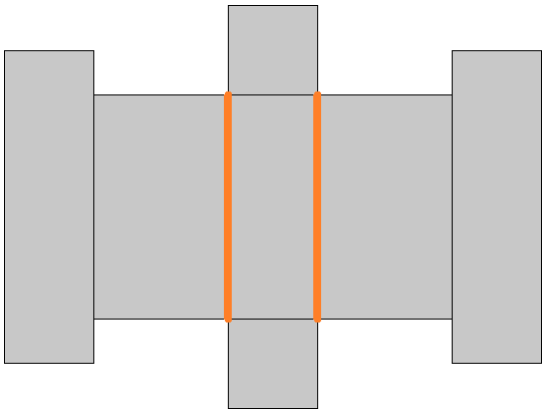

Figure 21. D2 - Ion-selective membranes on either side of the cross-flow channel

Single membrane version was feasible and more easily prototyped, but a completely separated cross-flow channel seemed as an attractive optimization (Figure 21). With limited time, prototyping the two-membrane version became less obtainable; however, simulations would still be possible. The channel parameters are shown in Table 7.

Table 7. D2 geometric parameters in COMSOL

	Intracellular Channel [mm]	**Extracellular Channel [mm]**	**Cross-Flow Channel [mm]**	**Channel Junction [mm]**
Widest meas. (x-axis)	0.010	0.010	0.004	-
Highest meas. (y-axis)	0.014	0.014	0.018	0.016

Simulation setup: Simulations were done using only water (H_2O) for the materials with similar principles applying as were for design 1. Both the initial and inflowing concentrations for the side-channels were derived from the combined biological and artificial principles. The initial concentration in the intracellular channel was set to 140 mol/m^3 and 10 mol/m^3 in the extracellular. The inflow concentration for the intracellular channel was 140 mol/m^3 and 5 mol/m^3 for the extracellular. The cross-flow channel's inflow concentration was set to 140 mol/m^3. The thin diffusion barrier(s) had a layer thickness of 1 µm and a diffusion coefficient ($D_{s,\,c}$) of 2.65E-10 m^2/s for positive ions. For verifying the cross-flow valve concept with various control signals with an excess of

settling times, a simulation window of 30 ms was set. Flow velocities of all channels for obtaining different voltage levels quickly within the typical AP voltage boundaries were found through only a few corrective trials. The velocities were found faster for design 2 because of the knowledge gained from design 1 simulations and the similar principles used by Timothée Levi and Teruo Fujii in their work [6]. The used velocities are shown in the following Table 8, Table 9 and Table 10.

Table 8. D2 intracellular normal inflow velocity control settings

Function Start [ms]	**Function End [ms]**	**Flow Velocity [m/s]**
0	10	-0.03
10	15	0.00
15	30	0.08

Table 9. D2 extracellular normal inflow velocity control settings

Function Start [ms]	**Function End [ms]**	**Flow Velocity [m/s]**
0	10	0.08
10	15	-0.03
15	30	0.08

Table 10. D2 cross-flow normal inflow velocity control settings

Function Start [ms]	**Function End [ms]**	**Flow Velocity [m/s]**
0	10	0.00
10	15	0.02
15	20	0.10
20	25	0.04
25	30	0.00

3.1.2 Optimized CAD Designs

The designs simulated in COMSOL presented a solid basis of design guidelines for real prototypes. The microfluidic chips were modelled using a CAD software called the Autodesk Inventor Professional 2018.

Two types of models were made. Each one in the general image of their respective simulation design. Due to the printing resolution limitations and ideally simplified 2D

simulations, it became impractical to draw the CAD models as the exact copies of the simulation designs. Even so, real-life experimental process demanded several trials and several iterations before any results were obtained. The differences between the first and last iteration CAD models of design 1 are presented in Table 11.

Table 11. Design 1 CAD model measurement comparison between revisions 1 and 5

	1CT [mm]	**1HT [mm ± dif.]**	**1CB [mm]**	**1HB [mm ± dif.]**
Length	25.00	25.00 (± 0.00)	25.00	25.00 (± 0.00)
Width	15.00	15.00 (± 0.00)	15.00	15.00 (± 0.00)
Thickness	1.50	1.50 (± 0.00)	1.50	1.50 (± 0.00)
Inlet/outlet (height)	4.50	4.50 (± 0.00)	4.50	4.50 (± 0.00)
Inlet/outlet (external width)	2.00	2.00 (± 0.00)	2.00	2.00 (± 0.00)
Inlet/outlet (internal width)	1.25	1.25 (± 0.00)	1.25	1.25 (± 0.00)
M3 support holes	3.50	3.50 (± 0.00)	3.50	3.50 (± 0.00)
Diameter of channel reservoir	3.00	3.00 (± 0.00)	3.00	3.00 (± 0.00)
Electrode groove (width)	2.00	2.00 (± 0.00)	2.00	2.00 (± 0.00)
Electrode groove (depth)	0.35	0.35 (± 0.00)	0.35	0.35 (± 0.00)
Channel width	0.30	0.30 (± 0.00)	0.30	0.30 (± 0.00)
Channel depth	0.30	0.30 (± 0.00)	0.30	0.30 (± 0.00)
Channel length (excl. reservoir)	11.015	11.015 (± 0.00)	2.458	2.458 (± 0.00)
Channel boundary (width)	0.40	0.40 (± 0.00)	0.50	0.55 (+ 0.05)
Channel boundary (depth/height)	0.30	0.30 (± 0.00)	0.40	0.40 (± 0.00)

What can be seen from Table 11, is that the changes (emphasized with coloured boxes) over multiple iterations of the design 1, were subtle regarding parameters. Optimisations were made to essential features which improved the top and bottom chip alignments and

the chip's assembly process. More noticeable changes of the design 1 can be seen from the compared CAD model images on Figure 22, Figure 23, Figure 24 and Figure 25.

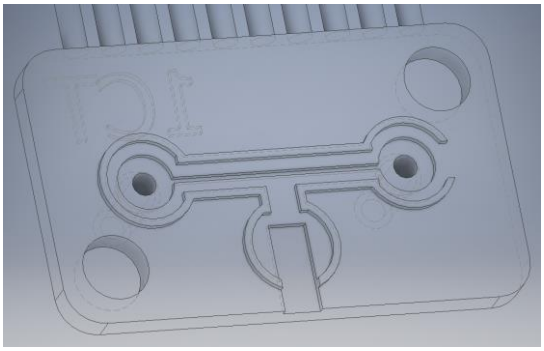

Figure 22. D1 top-side (1CT), revision 1

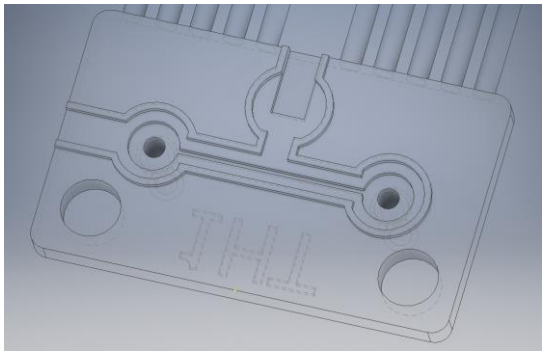

Figure 23. D1 top-side (1HT), revision 5

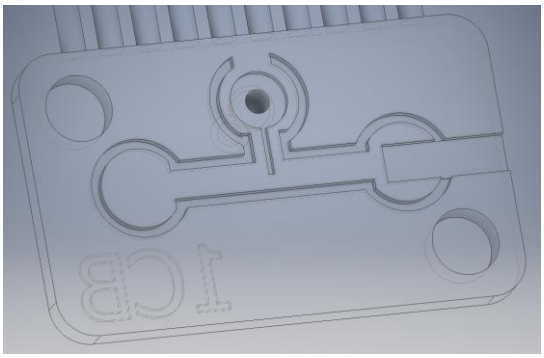

Figure 24. D1 bottom-side (1CB), revision 1

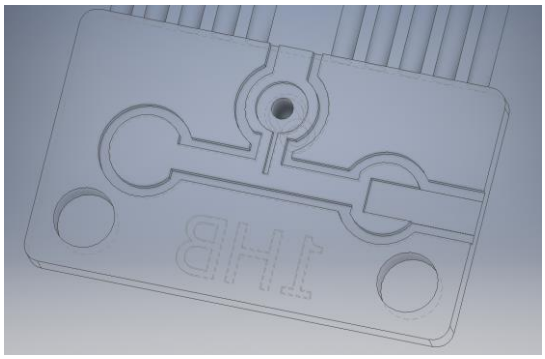

Figure 25. D1 bottom-side (1HB), revision 5

The four important features that ended up changing were the extension of the channel boundaries, the widening of the debossed channel boundary, the reorientation of the top-side chip and the relocation of an M3 support hole. The motivation for those changes was the numerous failed earlier revision chips with physical damage right after fabrication or during the assembly process.

Proceeding with design 2, differences between the first and last iteration CAD models are shown in Table 12 continuing the following page.

Table 12. Design 1 CAD model measurement comparison between revisions 1 and 5

	1CT [mm]	**1HT [mm ± dif.]**	**1CB [mm]**	**1HB [mm ± dif.]**
Length	25.00	40.00 (+ 15.00)	25.00	40.00 (+ 15.00)
Width	15.00	24.00 (+ 9.00)	15.00	24.00 (+ 9.00)
Thickness	1.50	2.50 (+ 1.00)	1.50	2.50 (+ 1.00)
Inlet/outlet (height)	4.50	5.60 (+ 1.10)	4.50	5.60 (+ 1.10)

	1CT [mm]	1HT [mm ± dif.]	1CB [mm]	1HB [mm ± dif.]
Inlet/outlet (external width)	2.00	2.00 (± 0.00)	2.00	2.00 (± 0.00)
Inlet/outlet (internal width)	1.25	1.25 (± 0.00)	1.25	1.25 (± 0.00)
M3 support holes	3.50	0.00 (- 3.50)	3.50	0.00 (- 3.50)
Diameter of channel reservoir	2.00	3.00 (+ 1.00)	3.00	3.00 (+ 1.00)
Electrode groove (width)	2.00	2.00 (± 0.00)	2.00	2.00 (± 0.00)
Electrode groove (depth)	0.35	0.35 (± 0.00)	0.35	0.35 (± 0.00)
Channel width	0.30	0.60 (+ 0.30)	0.30	0.60 (+ 0.30)
Channel depth	0.30	0.60 (+ 0.30)	0.30	0.60 (+ 0.30)
Channel length (excl. reservoir; cross-flow)	10.787	25.061 (+ 14.274)	-	-
Channel length (excl. reservoir)	5.787	13.758 (+ 7.971)	5.787	13.758 (+ 7.971)
Channel boundary (width)	0.204	0.60 (+ 0.396)	0.285	1.00 (+ 0.715)
Channel boundary (depth/height)	0.30	0.50 (+ 0.20)	0.40	0.60 (± 0.20)

Contrary to the first design, design 2 changes (emphasized with coloured boxes) radically over the course of its iterations. Using comparable, upscaled models as templates for both designs did not work. The added complexity of handling three closely positioned channels over two channel layers required more space to fit the channel boundaries and increased feature sizes to have less dependance from the fabrication equipment limits and tolerances. By increasing the size of relevant parameters, the upscaling of the channels remained tied to the simulation models. On the other hand, changes in parameters such as thickness and the removal of M3 support holes were motivated by the chip fabrication failures seen with initial revisions of both design. Aside from fabrication, the matching of the top and bottom chips during the assembly could cause an unwanted low yield and high scrap rates of fully assembled design 2 chips. After this explanation, the noted design

flaws could be better illustrated and noticed by looking at the CAD model images with the added knowledge (Figure 26, Figure 27, Figure 28 and Figure 29).

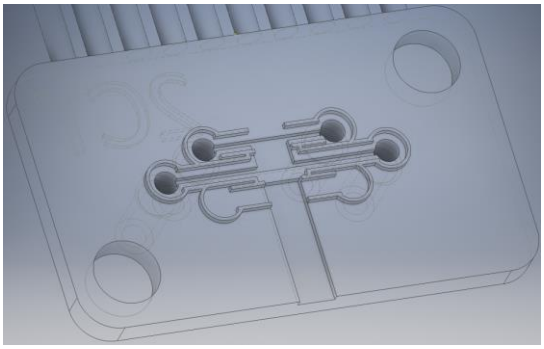

Figure 26. D2 top-side, revision 1

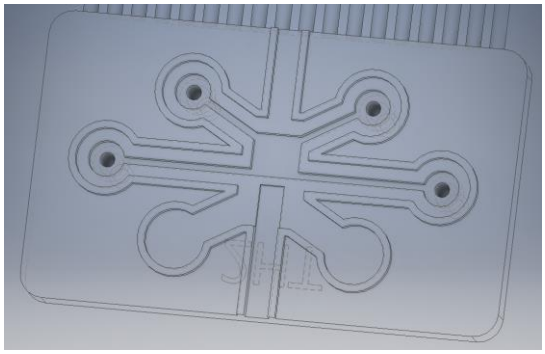

Figure 27. D2 top-side, revision 5

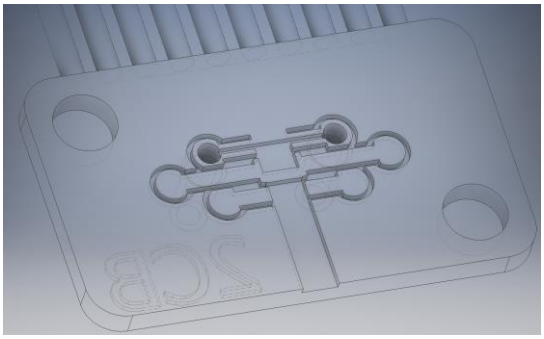

Figure 28. D2 bottom-side, revision 1

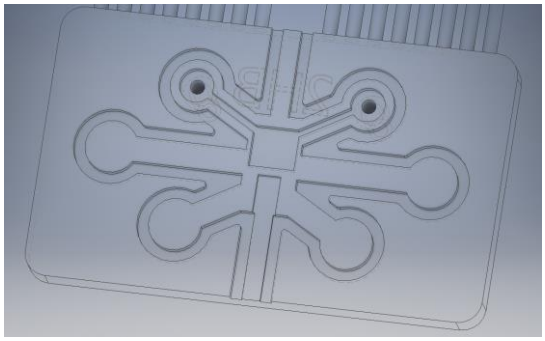

Figure 29. D2 bottom-side, revision 5

It is important to note that the D2 depicted on Figure 26, Figure 27, Figure 28 and Figure 29 uses the one membrane sheet method. The use of a second membrane interface would result adding further complexity to the design. By comparing the earliest and latest revisions of design 2 side by side, it's easy to see the, now clear, limitations appearing from revision 1. To keep the upscaling ratios of channel junctions, close to the simulation designs, the CAD modelling rules needed to be more flexible, resulting in angled side-channels. This concludes the overview into the CAD modelling of microfluidic chips for artificial neurons. Both D1 and D2 revision 5 CAD models would be used in experiments

3.2 Evaluation of Prototyping Options

3.2.1 Actuators

Before the cross-flow valve was selected as the most convenient and fastest obtainable valve option, various other design ideas were considered with different valve options in mind. In addition to the previously mentioned cross-flow valve and quake valve solutions, proposed solutions included using a single relay to create rapid enclosure of the external

channels or two relays in conjunction over an external tubing. The latter would work by firstly blocking the flow in the tube with one relay. After that, the switching of the second relay on the enclosed channel between the blockage and the inlet would cause a rapid increase in pressure, consecutively creating a small pulse in flow velocity towards the chip. Besides the more obtainable options, papers have been written on the use of actuators built into microfluidic chips. For instance, a PDMS microfluidic chip having a slot cut out or open surface above the channel [13]. The slot is then filled with a permalloy which would actuate the lower cavity when external magnetic fields were applied [13]. The magnetic micropump principle is shown on Figure 30.

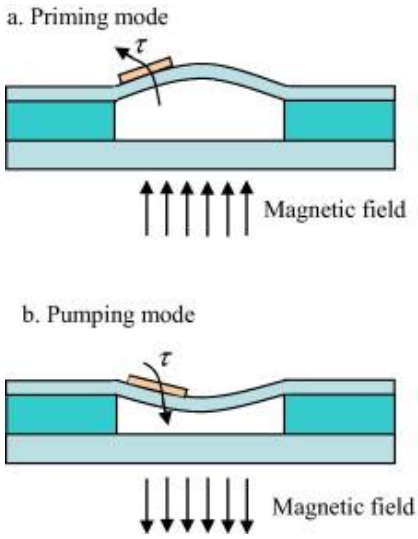

Figure 30. Magnetic micropump above the channel of a PDMS microfluidic chip [13]

The article “An integrated planar magnetic micropump” by Junhui Ni et al. included also a valve option, yet again built into a PDMS chip [13]. The channels would require ridges with varying widths for different degrees of flexibility (Figure 31).

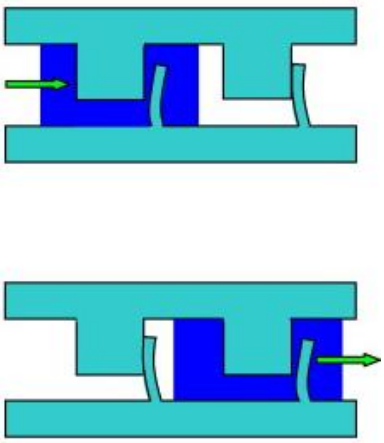

Figure 31. Flexible PDMS unidirectional flow valves [13]

Even though both the PDMS flow valve and micropump options are excellent for micro-precision controls, both require the use of soft chip materials and the feature sizes would remain out of reach with the available equipment. Many other options are offered by a popular high performance microfluidic equipment provider called Elveflow. They offer microfluidic valve matrixes, sequential injection valves, syringe-, pressure- (see example on Figure 32), vacuum pumps and even OEM solutions.

Figure 32. Elveflow high performance microfluidic OB1 Pressure Controller Mk3 [14]

To use more conventional actuators like a cross-flow valve with no internal features to speak of and syringe pumps, which are be cheaper, are more flexible and favourable. Syringe pumps are continuously advancing along with microfluidics to become more accurate and oscillation proof. However, their switching rate is slow.

3.2.2 Chip Fabrication

When fabricating microfluidic prototypes, there are several different options to choose from. Silicon microfabrication has been the most popular since the beginning of microfluidics due to its wide availability in the electronics industry. But the applications for microfluidics often require less costly and more specialised solutions. If a microfluidic device were intended to be integrated into a sensory system where chip transparency was a requirement, milling (otherwise known as bulk micromachining) channels into a glass surface would be best suited. However, milling into glass at microscales is still relatively expensive, there aren't many providers for such services and the manufacturing time is long. Along with milling, there are common techniques such as the standard photolithography, hot embossing and chemical etching that can be used on a glass substrate [15]. While continuing to look beyond the disadvantages of the initial glass chip production, to complete a microfluidic device, it requires a second layer, which would

enclose the channels, i.e. the sealing layer. The secondary layer can be glued, thermally fused in high temperatures or melded together with UV epoxy resin at room temperatures [16]. The cheapest method of gluing, as is often the choice, carries along a higher chance of leakage gaps in the assembly. As a countermeasure, the number of duplicate prototyping chips could be increased, thus encouraging to look for faster and more inexpensive chip manufacturing options.

Aside from solid, expensive structures, there are two, more common, soft technologies – PDMS soft lithography and 3D printing. A precision mould would typically be made of glass or silicon, but with an advantage compared to its inverted option. Using a cheaper material over a glass mould would enable producing any number of casted chips much faster and cheaper. The reproduction quality will however be limited only by the accuracy and repeatability of the casting process. An accompanying problem with casting is an increased chance of chip failure due to the common occurrence of air-bubbles intrinsically created during casting. As polydimethylsiloxane (PDMS) has become more widely available, it has been often used as the substance for casting chips, enabling feature sizes as low as 6 nm. On the other side, the 3D printing industry has been growing at a rapid rate. Printed microfluidic chips can also be used as moulds but in comparison to glass moulds, higher levels of precision come at a much higher cost. 3D printers suitable for microfluidics can start from as low as 1,000 € (used) and reach well beyond 10,000 €. Thus, making this method more feasible only if a printer was already available. As with glass, 3D printed structures can be either channelled chips or their inversions as moulds. Regardless, the decisive feature of 3D printing is that the manufacturing times can be significantly reduced in comparison to all previously mentioned options. A few of the faster commercially available resin based 3D printer examples include NP1 by NewPro3D and Carbon M1 by Cabron3D, bringing printing speeds to around 200 mm/h by using technologies called Intelligent Liquid Interface (ILI) and Continuous Liquid Interface Production (CLIP) respectively. In comparison, the older more common SLA and DLP type printers such as P4 Standard LED by EnvisionTEC works at 25 mm/h and the P4 Standard printer provided by TUT at 8 mm/h.

High fabrication speed can be a convenience, but features like this are the guidelines towards the most suitable prototyping option [15]. When aiming to produce prototypes for something as far out of the ordinary as is an artificial neuron, the number of unknown

variables and obstacles define the course for choosing the prototyping method. The optimal solutions ought to fill the following requirements:

- Low cost
- Fast fabrication
- Fast assembly
- Solid material

The lower the cost, the larger the number of prototypes made on a budget. The faster the fabrication and assembly, the larger the number of prototypes made within a limited timeframe. These requirements quickly eliminate micromachining, photolithographic and hot embossing methods from proposed options. As also mentioned by T. Levi and T. Fujii, softer materials are always at a disadvantage when dealing with pumps and pressures as they tend to crack [6]. Due to having simulated with relatively high liquid flows and having direct goals to induce pressure makes this a relevant matter. To avoid any additional issues with this topic, the solid material requirement was included, consecutively removing any moulding related option together with the problems of air-bubbles. The optimal remaining option was 3D printing.

CAD models, explored in paragraph 3.1.2, were printed by an earlier model of EnvisionTEC's Perfactory 4 Standard 3D printer, to which access was provided by Tallinn University of Technology. The specifications of the printer were suitable for microfluidics due to its high printing resolution of about 50 μm (Table 13).

Table 13. EnvisionTEC Perfactory 3D printer properties [17]

Machine Properties	**Value**
Printing resolution	~50 μm
Building envelope	160 x 100 x 180 mm
Projector resolution	1920 x 1200
Data handling	STL
Printing method	DLP
Average printing speed	~8 mm/h (50 μm voxel thickness)
Resin	LS600

Printing resolution is normally tied to the types of resins used. The codenamed printing material LS600 provides a good segue into the next paragraph.

3.3 Evaluation of Structural Materials

LS600 is one of many 3D printing resins, but there is also another type of printing material called filament. Resin is normally more expensive than filament, but its higher printing accuracy and less noticeable layer bands are two critical reasons why resin is more suited to fabricating a microfluidic device. More precise printing reduces the chances of fluid leakages. The relevant properties of the used resin LS600 are shown on Table 14.

Table 14. 3D printing resin LS600 relevant properties [18]

Property	**Value**
Shore hardness	85, D
Density	1.10 g/cm^3
Appearance	Opaque yellow-beige

Because of the microfluidic channels being split onto two chips in CAD designs, the first and second layer are both functional, yet acting also as sealing layers for each other. This enables opting to use one of the simplest and cheapest sealant types which is glue. However, gluing is accompanied by a danger of disabling the porous membrane if they came into contact. But the use of channel boundaries helps to reduce the chances of that happening.

While choosing the porous membrane, it was required to be at least as effective as the Nafion membrane used in the device made by T. Levi and T. Fujii [6]. Options for off-the-shelf ion selective porous membranes were slim and a good comparative study made by G. Hernández-Flores et al. showed that the alternative agar membranes produced only about 40 % of the efficiency compared to Nafion 117 [19]. Thus, Nafion was still chosen and a kit including Nafion XL, Nafion 212, Nafion 115 and Nafion 117 was acquired. The thicknesses of the Nafion membranes are shown on Table 15.

Table 15. Acquired Nafion membrane sample thicknesses

	Nafion XL	**Nafion 212**	**Nafion 115**	**Nafion 117**
Thickness	27.5 µm	50.8 µm	127 µm	183 µm

Aside from the use of the more expensive resin and Nafion membranes, the electrodes were chosen based on their cost and obtainability. Due to the various CAD designs and chip sizes, differently sized electrodes would be required. For this reason, a pure metal sheet option was optimal. This however, removed gold and platinum as options. RS Pro, Hard Drawn High Conductivity (HDHC) copper sheet was chosen [20].

3.4 Experimental Setup

After arriving at acceptable designs to prove the concept of an artificial neuron in a microfluidic chip, efforts towards choosing the prototyping method, subsequent materials for the fabrication and assembly were made. Selections included 3D printing as the prototyping option, LS600 resin as the fabrication material and off-the-shelf super glue for the assembly. The experiments were conducted in a conservative laboratory environment with the included necessary equipment, both provided by TUT. This paragraph is divided into 3 parts in which the build-up towards the experimental measurements includes several system concepts, fabrication and assembly processes as well as descriptions of external equipment used.

3.4.1 System Concepts

All experiments were done with the purpose of proving that the simulated results could be replicated with 3D printed microfluidic chips. Even so, the experimental methods fell into two categories – manual and automated. Setup diagrams for the manual fluid flow manipulations of design 1 is presented below on Figure 33.

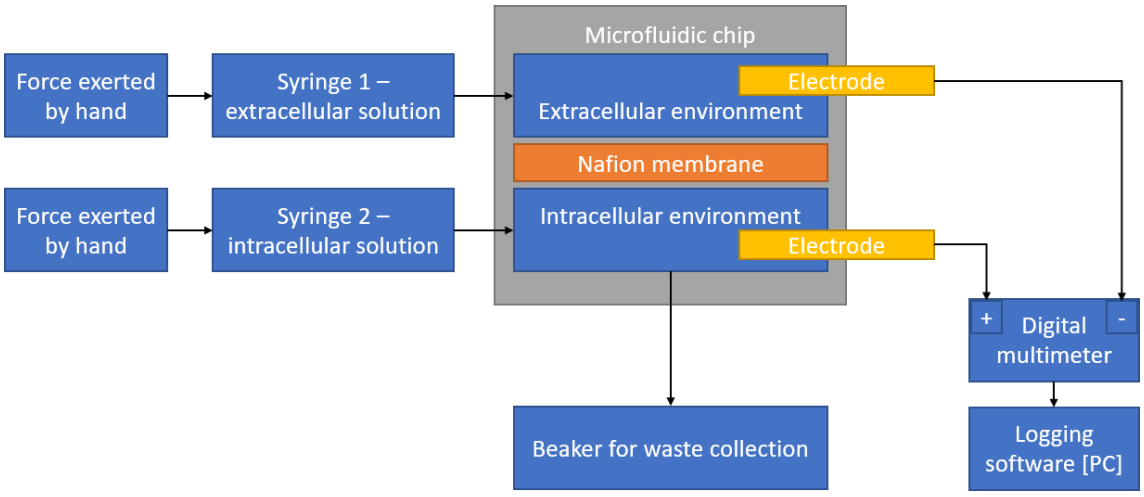

Figure 33. System diagram of the manual experimental setup for D1

With the least number of elements, manual experiments on D1 were promising. With the second design on the other hand, clear limitations arose when simultaneous control over all three channels was required (Figure 34).

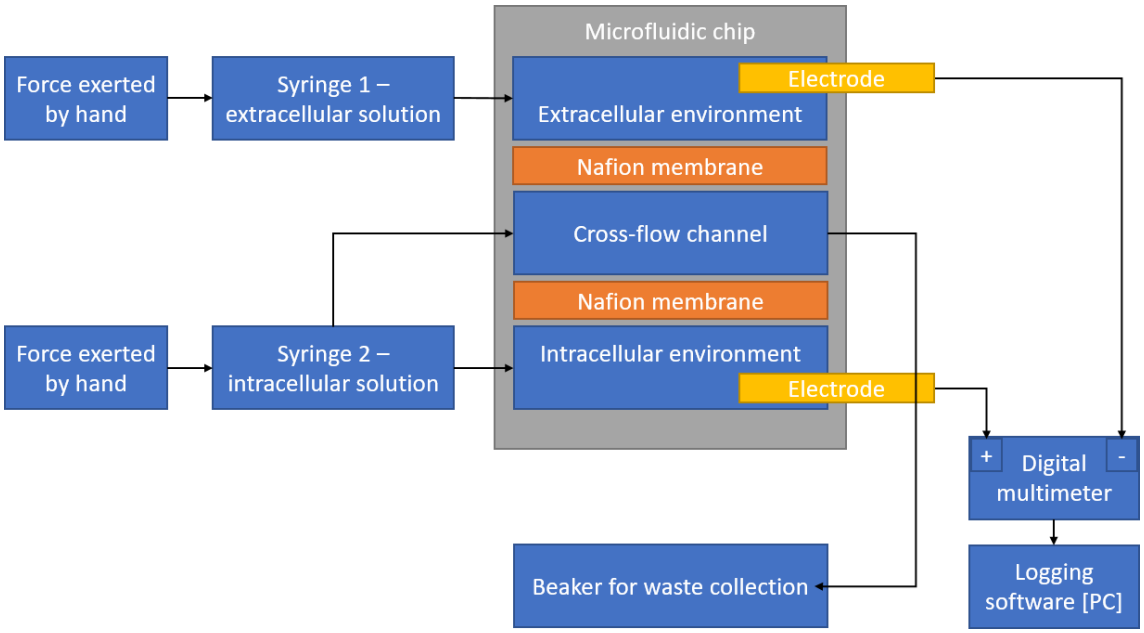

Figure 34. System diagram version 1 of the manual experimental setup for D2

Due to having three different channel another version of the manual system diagram shown on Figure 34 was proposed. This meant that the second version had the sole purpose of verifying the functionality of the cross-flow valve.

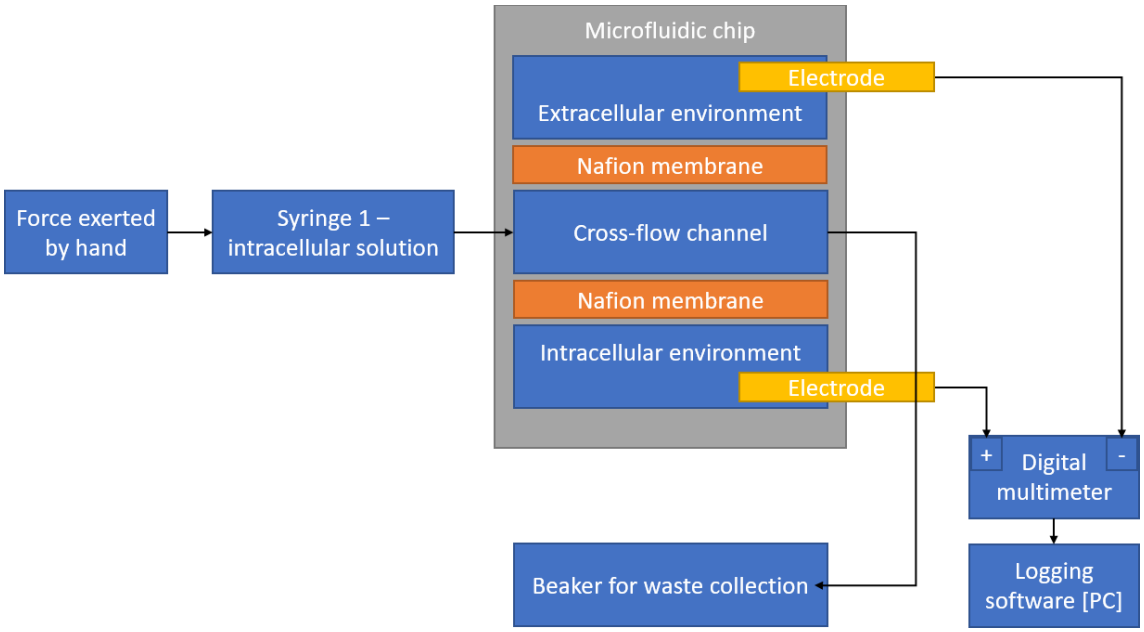

Figure 35. System diagram version 2 of the manual experimental setup for D2

Version 2 (Figure 35, Page 44) removed the requirement for three separate flow controls, but required assumptions that the intra- and extracellular environments in the microfluidic chip were prefilled and sealed. Additional assumptions were made, that while the cross-flow channel remained clear of any liquid substance, no voltage gradient would be present between the intra- and extracellular environments. Even though various approaches were considered, the timeframe for this thesis was limited. Experiments with D2 were bound only to manual attempts due to the surfacing of critical complications, which are detailed further in paragraphs 3.4.4 and 4.2. In contrast, the endeavours to automate the system with D1 were more favourable.

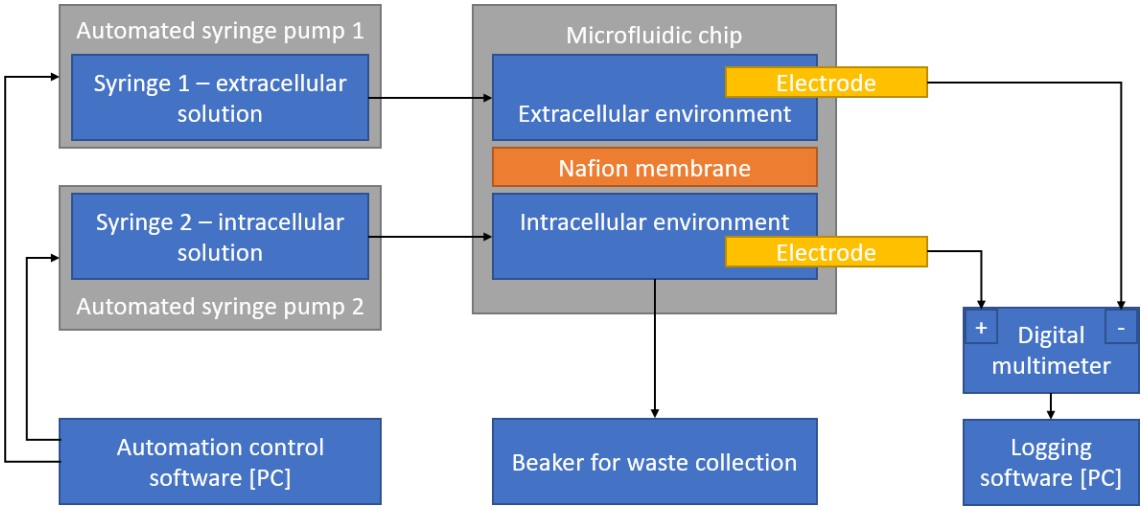

Figure 36. System diagram of the automated experimental setup for D1

The automated system displayed on Figure 36 shows the use of separate pumps for each syringe, but their simultaneous control through a specialised software on the computer. After reviewing the different experimental system configurations, system components were needed to be acquired.

3.4.2 Fabrication & Assembly

Initial steps for 3D printing required CAD file conversions into device-acceptable STL-file formats. The STL files were built with an average count of 5000 triangles by choosing the medium resolution in CAD file export settings of Autodesk Inventor. Higher resolutions caused visible failures in the printing results. Lower resolutions, on the other hand, caused curvatures to become noticeably segmented, leading to misalignments of top and bottom layer channel boarders. The STL files were uploaded to the computer linked with the 3D printer. STL files were then loaded into EnvisionTEC's Perfactory Software Suite 2.6 (PSS). The virtualised building platform of the 3D printer was

populated by the automated placement function included in PSS. Automated placement capability of PSS was acceptable, on the other hand, rotations were not always accurate, which pressed for additional manual revising. Having different chip footprints of 1.62 cm^2 and 3.402 cm^2 combined with a safe clearance distance of 25 mm, the number of single-sided chips per batch was limited to 12. An example layout of 12 single-sided chips on the graphical printable building platform is shown in Figure 37.

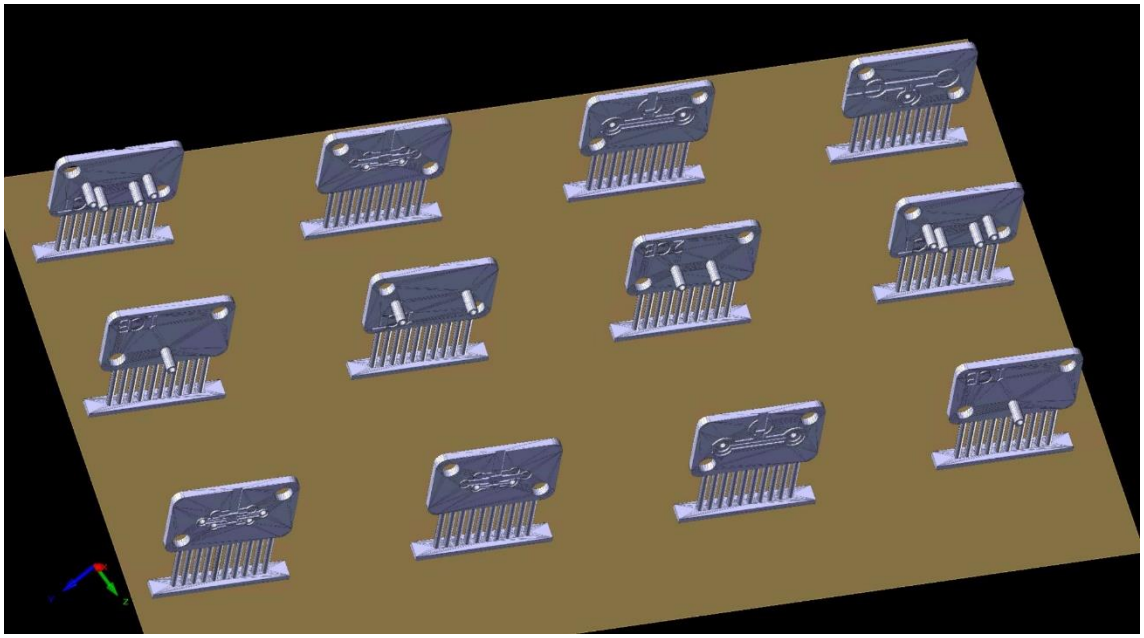

Figure 37. 3D printer's graphical building platform in PSS, filled with three examples of each different microfluidic chips

At the end of every printing job, the building platform together with the chips are lifted out of the printer. The chips are then individually cut off from the solidified surface layers through the supporting columns. Thinner support columns enable cutting to be done quickly with regular scissors. Removed chips are placed into a cleaning bath such as isopropyl alcohol (IPA). After soaking the chips in IPA for about 2 to 3 minutes, the chips can then be placed into water to wash off the alcohol and other residual resin wastes. Two cycles in IPA and water are sufficient for rapid prototyping. Cleaned chips are dried and their channels cleaned from any remaining chunks of residue with the help of a thin needle. Visual verification continues by checking the integrity of the chip's channels and channel boundaries. There is a degree of tolerance regarding defects in channel boundaries. Smaller defects could be overlooked if the cavity remains smaller than the surface tension of the sealant. More severe defects were often common on only one, top or bottom side of the chip design, deeming their counterparts unusable as well. Because of this, after visual verification, the average acceptable remainder was close to 50% of

the total batch. The low success rate of fabrications was partly due to artefacts introduced by the printer as well as the rigidity and small size of chips, often leading to breakage. Chips which passed the visual verification, are measured and compared with their respective CAD models to record the printer's tolerances with LS600 resin. A multitude of tolerance measurements were made, from which two more noteworthy examples are shown on Table 16 and Table 17.

Table 16. Tolerances of D1 top side chip from batch 1

Feature sizes > 1 mm	**Tolerance [%]**		**Feature sizes < 1 mm**	**Tolerance [%]**
Length	0.24		Channel width	3.33
Width	1.80		Channel boundary	13.75
Thickness	6.67			-
M3 support hole	6.86			-
Inlet/outlet (height)	2.67			-
Inlet/outlet (width)	1.00			-
Diameter of channel reservoir	4.33			-
Electrode groove (width)	1.00		Electrode groove (depth)	2.86

Table 17. Tolerances of D1 bottom side chip from batch 1

Feature sizes > 1 mm	**Tolerance [%]**		**Feature sizes < 1 mm**	**Tolerance [%]**
Length	0.16		Channel width	3.33
Width	1.87		Channel boundary	5.00
Thickness	4.00			-
M3 support hole	9.14			-
Inlet/outlet (height)	1.55			-
Inlet/outlet (width)	5.00			-
Diameter of channel reservoir	4.33			-
Electrode groove (width)	0.50		Electrode groove (depth)	2.86

The data of the example tolerance tables were taken from chips in the first batch. Tolerance tables can give good insight into which feature sizes might require more

attention. Fortunately, tolerances of critical features such as channel width, electrode groove size and channel reservoir diameter, all remain below 5 %. Features with tolerances between 5 and 20 %, such as the thickness of the chip, M3 support holes and the channel boundaries, are not as critical to the functionality of the microfluidic chip and are therefore acceptable. Nevertheless, channel boundaries must preserve their integrity and match with their inversions. Channel boundaries are also essential for guiding and preserving the placement of Nafion membranes. Having a multitude of Nafion membrane thicknesses to choose from, by being the thinnest, Nafion XL was used for all assemblies. Due to its fragility, it was the only membrane placed between a backing film and coversheet. Interestingly, all three layers are indistinguishably transparent and stuck together with no visible loose corners to help with the separation process. It was found that there can be more separation approaches in addition to the safe handling method [21]. Regardless, the middle layer was then carefully revealed (Figure 38).

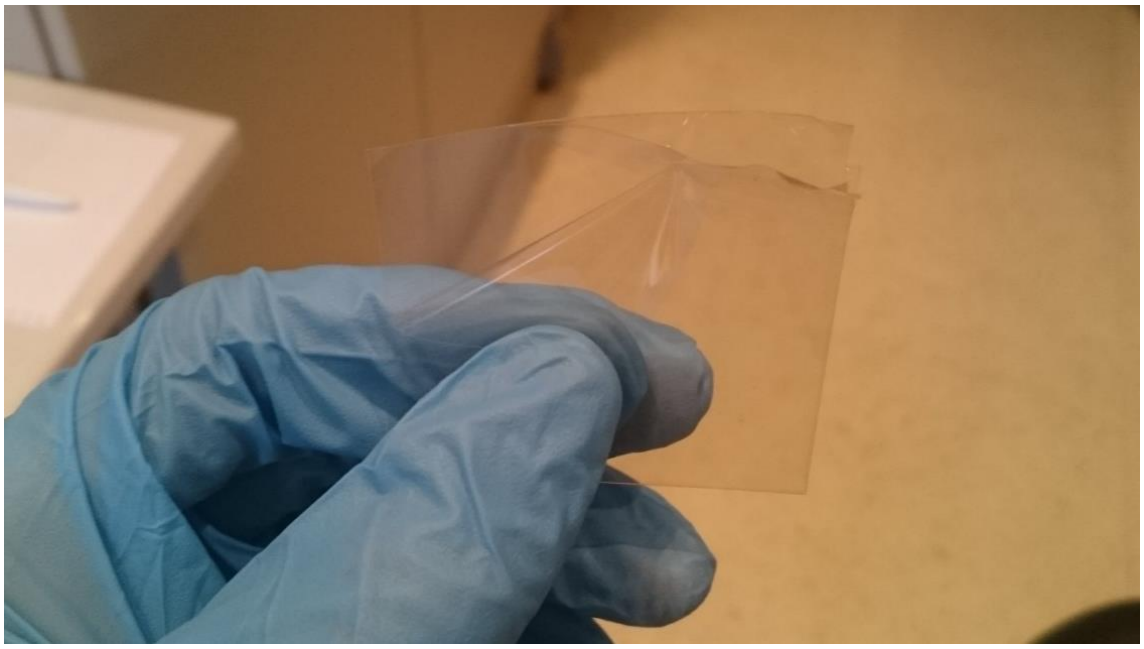

Figure 38. Revealed Nafion XL membrane between its backing film and coversheet

Thickness of the of the membrane was critical since it would be placed between two printed chips, each with its own channels. Thicker membranes would cause problems with the sealing of channels and create large leakage cavities in addition to unpredictable changes in channel parameters. Even with the thinnest 27.5 μm membrane, the chance of causing leakage cavities remained. Ideal placement of the membrane between the channel boundaries would help reduce the leakages. Multiple slices were cut for separate prototypes and with the help of tweezers, needles and a stronger light source, carefully

positioned between the channel boundaries and over the channel junction of the top side chip of the assembly. Stronger light source such as an LED flashlight was used to catch reflections off the membrane to visibly verify its location as can be seen on Figure 39.

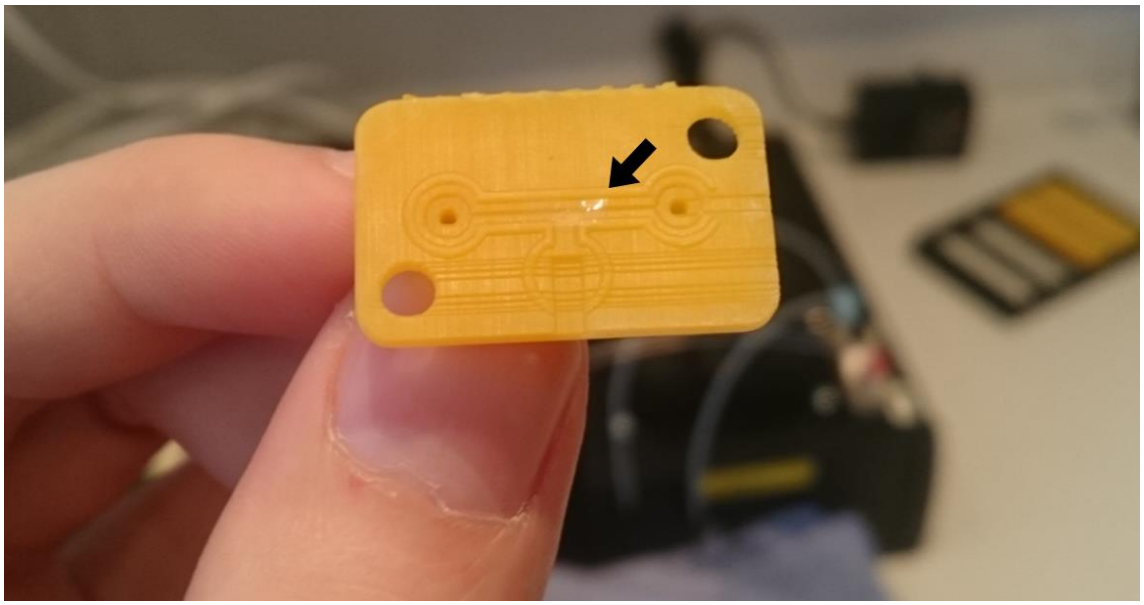

Figure 39. Nafion XL membrane reflection (location marked with a black arrow), indicating its correct position over the channel junction and between the channel boundaries of a D1 top side chip.

Aside from aiding with the Nafion membrane positioning, the main purpose of the embossed channel boundaries was to limit the spreading of the sealant into the channels and over the membrane during the assembly. After having placed the membrane, super glue was used to cover the top-side chip outside of the channel boundaries. The bottom-side chip was then carefully positioned over the other and slowly pressed together. The adhesion process took about ten minutes, after which the open electrode grooves were sealed by adhesive mounting putty, thus making the microfluidic chip ready for verifying the liquid handling capabilities of the opaque microfluidic assemblies.

1# Fluid test – Design 1: the bottom side inlet was sealed off with attaching a blocked tubing. A syringe filled with distilled water was connected to one of the inlets on the top side. Several liquid flow rates were manually tested. The top side chip's channel functionality was deemed adequate if there was minimal resistance against the flow through the channel and no leakages were detected around the sides of the chip.

2# Fluid test – Design 1: the bottom side inlet was reopened and the blocked tubing was attached to the open outlet on the top side. The syringe, filled with distilled water, remained in connection to the same top side inlet. Several flow rates were manually

tested. The bottom chip's channel and the membrane functionalities were deemed acceptable if there was now a considerable resistance against the flow through the channel, but still no leakages detected around the sides of the chip. Because the resin used for fabricating the chips is opaque, this second fluid test also helped to confirm that the porous membrane remained in place, both during the assembly and the first fluid test.

Fluid tests with the second chip design are analogous to the first. Every channel must be functional, the membrane must remain in place and no leakages around the chip can occur. After proving that the chips are usable, the adhesive mounting putty is removed from the electrode grooves, the channels flushed with air and left to dry. Meanwhile, HDHC copper electrodes were prepared. The 35 µm thick copper electrodes were cut to widths matching the electrode grooves, but longer in length to enable more convenient usability. After the chips had dried, prepared electrode strips were pushed into the electrode grooves and sealed with adhesive putty to prevent any leakages. An example of an assembled D1 microfluidic chip is shown on Figure 40.

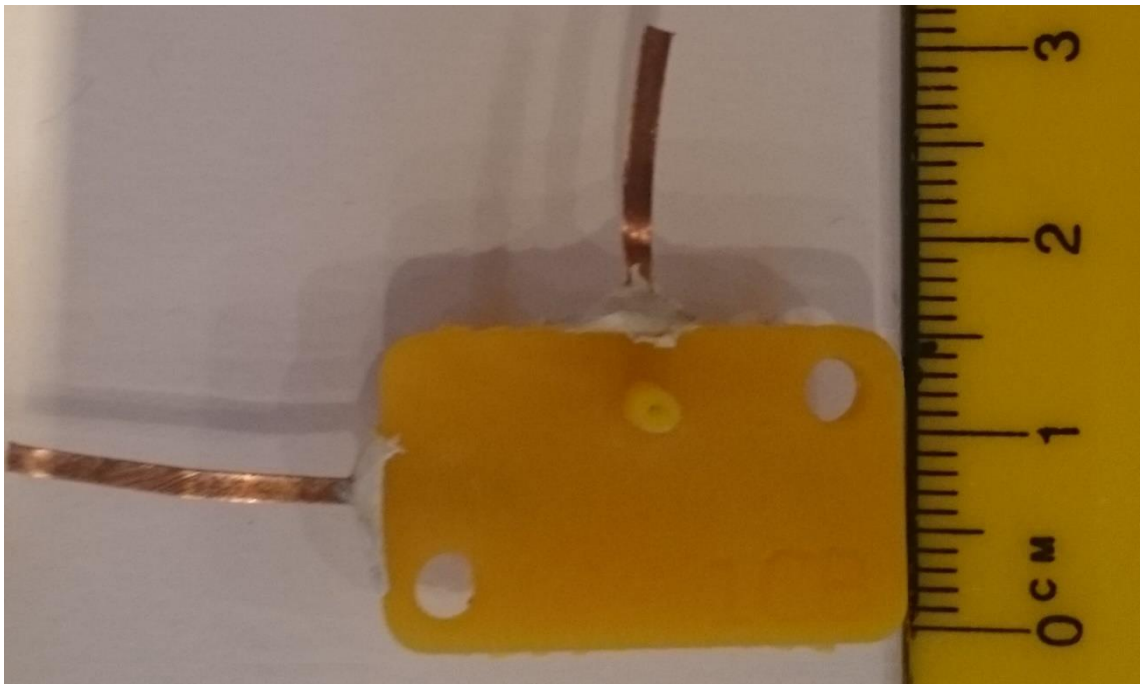

Figure 40. Fully assembled design 1 microfluidic chip

3.4.3 Test Equipment

As is shown in the system diagram depicted on Figure 36 (Page 45), the automation of the flow control of each syringe is done using a separate syringe pump. The available syringe pumps called netPumps by SpinSplit LLC were used (Figure 41, Page 51).

Figure 41. Remotely controlled syringe pump by SpinSplit LLC – netPump [22]

SpinSplit LLC offers a NI LabVIEW GUI, SpinStudio Flow Software, to gain simultaneous control over multiple devices using Ethernet connection. This combination offers a compact precision flow control and monitoring system proposing the chance to opt out of additional flow meters. Technical specifications of the netPump claim it having an accuracy equal to or less than 1 %, a maximum switching time of 10 ms, a minimum flow rate of 1 nL/min and maximum of 60 mL/min which should be more than enough after successful AP simulations with highest flow rates at 0.06 mL/s [22]. Another essential component in all system diagrams (Paragraph 3.4.1) is the digital multimeter. For this, Agilent 34410A digital multimeter was used (Figure 42).

Figure 42. Agilent 34410A digital multimeter - front view

Agilent 34410A digital multimeter has an accuracy of ± (0.003 % of reading + 0.003 % of range) at a DC voltage range of 100 mV [23]. The display offers 6.5-digit resolution with the lowest measurable voltage step of 0.1 µV at a rate of 31.7 % [23]. By connecting the multimeter with a PC via USB, it is possible to stream voltage measurements at rate of 100 samples per second and record them into a CSV file format. Faster readings are possible by recording directly onto the multimeter and uploading the dataset afterwards,

however fast visual feedback was required. The recording was done through a software multimeter built in LabVIEW (Figure 43).

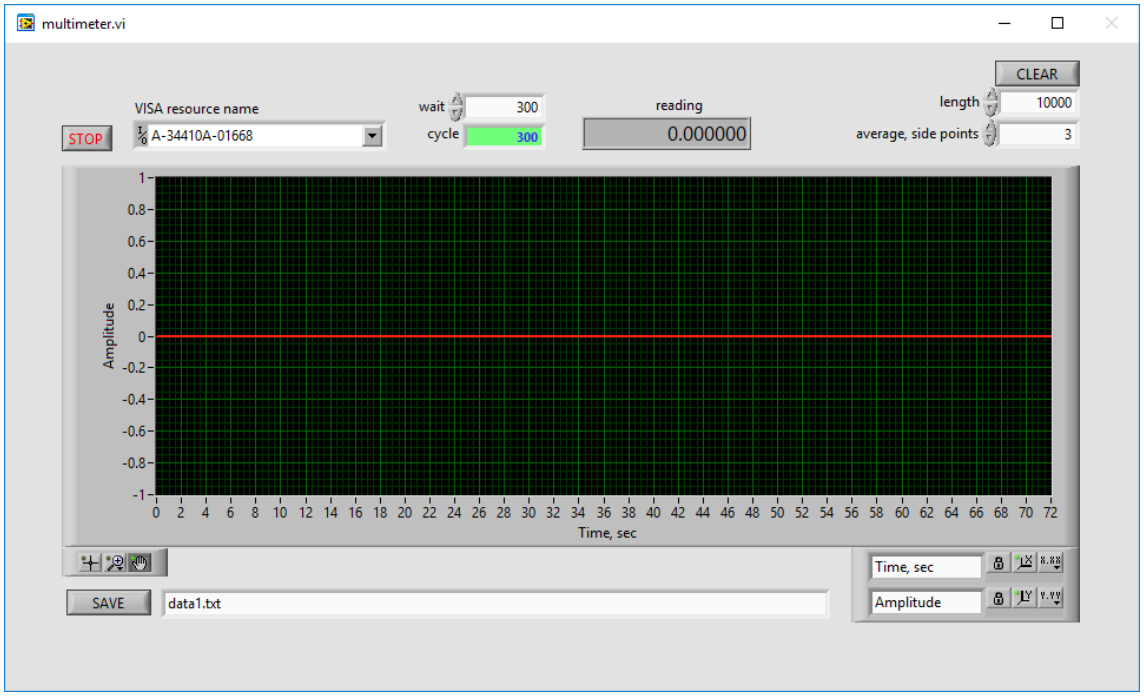

Figure 43. Graphical interface made in NI LabVIEW (multimeter.vi) for displaying and extracting recorded measurements from a benchtop multimeter (Agilent 34410A)

Aside from the larger external system elements, plastic 3 mL luer slip syringes were used. Syringes were connected to the microfluidic chips using Teflon (PTFE) tubes with diameters of 0.3 mm. Since PTFE tubes would not fit around the nozzle of a luer slip syringe, luer dispensing tips were used to get around that problem (Figure 44).

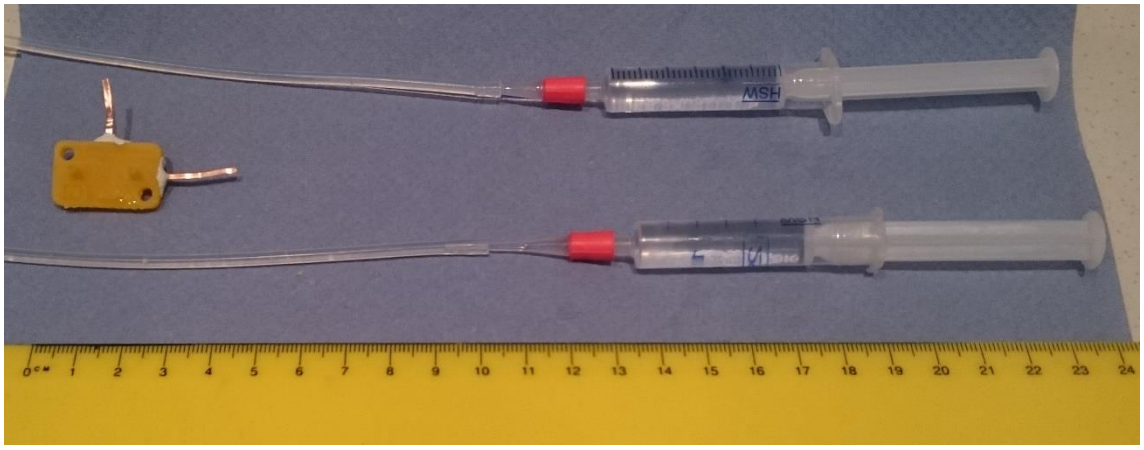

Figure 44. Syringe assembly with luer dispensing tips and Teflon tubing together with an assembled microfluidic chip of D1 over a ruler for scale reference

Less essential equipment, included items such as beakers, probes, standard GL45 reagent bottles and a Velleman VTBAL30 mini scale.

3.4.4 Measurements

Solutions for the measurements were prepared with pure materials. Two types of salts were tested – NaCl (99.97%) and LiBr (99.99%). Relevant properties of both salts are given on Table 18.

Table 18. Relevant properties of salts NaCl and LiBr

Property	**NaCl**	**LiBr**
Cation ratio by mass	0.3933	0.0799
Cation molar mass	22.990 g/mol	6.941 g/mol
Salt molar mass	58.440 g/mol	86.845 g/mol
Enthalpy of solution @ 25°C	+3.87 kJ/mol	−48.76 kJ/mol
Solubility in water @ 20°C	35.9 g/100 mL	166.7 g/100 mL

For each salt, two separate solutions with differences in substrate concentrations were made. Substrate concentrations used were 140 mmol per 1 mol of water for the intracellular and 5 mmol per 1 mol of water for the extracellular. A mini scale (Velleman VTBAL30) with a resolution of 0.01 g was used to weigh salts and water. By using the LiBr molar mass from Table 18, the mixing ratios with distilled water (molar mass of 18 g/mol) were calculated:

- 140 mmol LiBr in H_2O @ 25°C – ratio of 12.16 ± 0.01 g to 18 ± 0.01 g
- 5 mmol LiBr in H_2O @ 25°C – ratio of 0.43 ± 0.01 g to 18 ± 0.01 g

By using the NaCl molar mass from Table 18, the mixing ratios with distilled water were calculated as follows:

- 140 mmol NaCl in H_2O @ 25°C – ratio of 8.18 ± 0.01 g to 18 ± 0.01 g
- 5 mmol NaCl in H_2O @ 25°C – ratio of 0.29 ± 0.01 g to 18 ± 0.01 g

The soluble amounts of LiBr were roughly 48% larger than NaCl, which would seem as a more difficult mixing task at room temperatures. However, the solubility of LiBr at 20°C in water is about 464% of that of NaCl. This is due to the negative enthalpy of solution property of LiBr [24]. When a substance with the described property would come into contact with water, heat would quickly be produced during the ionisation process. The higher amounts of heat generated by adding LiBr to water causes the salt to fully

dissolve at a self-propelled increasing rate. In contrast, the positive enthalpy of solution of NaCl at RT requires heat from the solution to fully ionise. This could prove to be a problem if the solution is left with undissolved traces of crystals.

To proceed with the measurement process description, two 3 mL syringes were filled with prepared 140 mmol and 5 mmol ionic solutions. Syringes were connected to the microfluidic chip by the extended PTFE tubing, with the 140 mmol syringe attached to the intracellular inlet feature and the 5 mmol syringe attached to the extracellular inlet feature. Multimeter crocodile clip probes were attached to the electrodes, positive clip to the intracellular electrode and negative to the extracellular electrode. Lastly, the outlet feature(s) were connected to a waste beaker with additional PTFE tubing, completing the system diagram of the manual experimental setup.

In contrast to the linear flow signals that were used in the simulations, manual handling of the syringes would pose difficulties such as undefinable flow rates, slow actuation speeds, non-reversible flows, unsteadiness and non-repeatability. As a result, only characteristical shapes and voltage levels were sought. All recordings were made by the custom LabVIEW graphical user interface – multimeter.vi (Figure 43, Page 52). To obtain measurements with the automated system, syringes were fastened into the syringe pumps (netPump) and SpinStudio Flow Software was set up. NetPumps only enabled the automation of controlling the flow rates. Therefore, some manual interfacing was still required for creating pulses with desired shapes. Several different measurements were made throughout the time window of this thesis, in which several iterations were tested to achieve demonstrable results. Between every different type test, the microfluidic chip, PTFE tubes and syringes were flushed with distilled water, setting a clean stage for new experiments and results.

4 Results & Discussion

To discuss results of two different methods and provide general overview of the processes involved, the paragraph was split into three. Simulation and experimental results will be presented and analysed in succession. And finally, results are put into perspective.

4.1 FEA Simulations

With COMSOL D1 design, the AP shapes were sought. Successful attempts were made with the presented parameters (Paragraph 3.1.1).

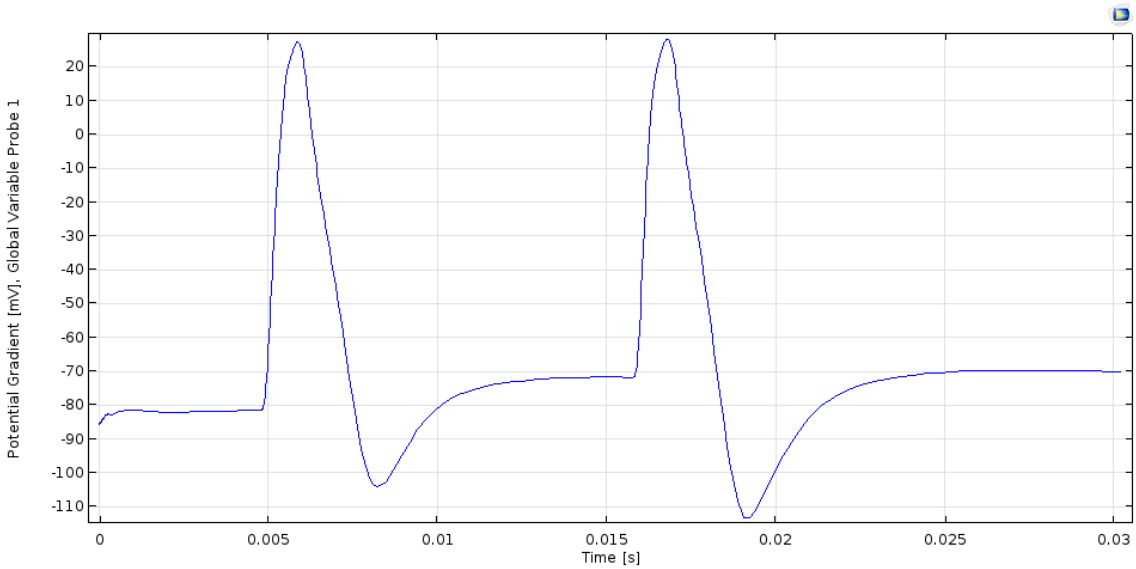

Figure 45. COMSOL simulation results; D1 5 ms AP generation with 2 consecutive pulses; highest depolarization achieved at 28.28 mV; lowest hyperpolarization achieved at -113.44 mV

Pulses shown on Figure 45, calculated from the Nernst equation as detailed in paragraph 2.1.2, were generated by a combination of push-pull inflow signals. Design 1 inflow velocity signals (Table 5 and Table 6, Page 29) are graphically represented on Figure 46.

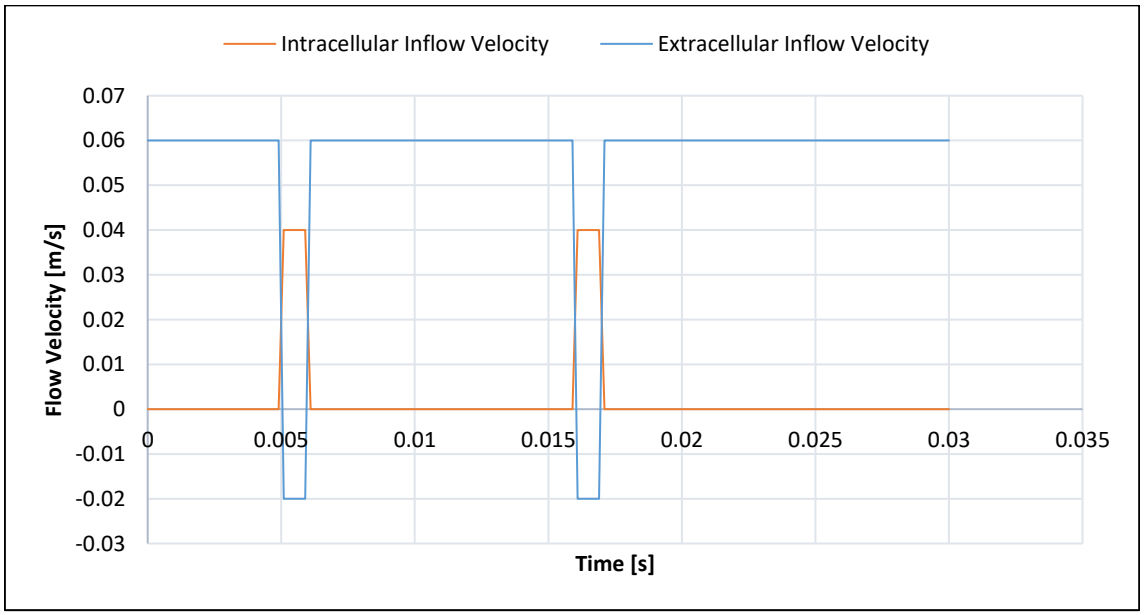

Figure 46. Graphical representation of inflow velocities in D1 AP pulse simulations

For a better representation of the concentrations and flow velocities, on Figure 47 the resting state before the first pulse was held during the simulation time of 4.0 ms, by keeping a constant flow through the extracellular environment.

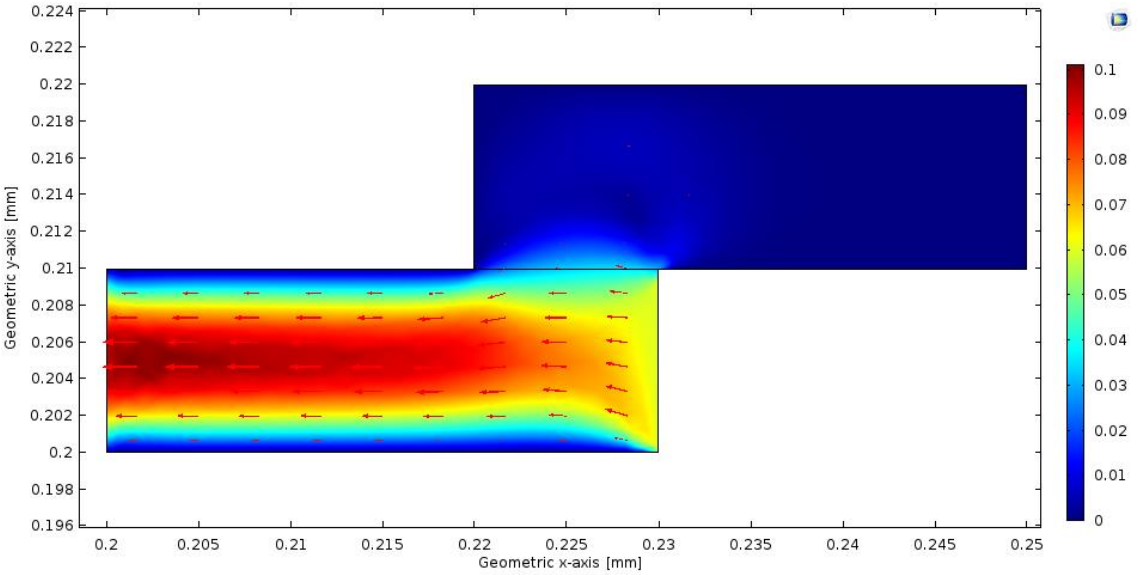

Figure 47. COMSOL D1 Flow velocities during the maintaining of the resting state (time 4.0 ms); flow velocities are weighed with colours which are described by the legend on the right of the graph (m/s)

Having close to zero flow in the intracellular channel, a pressure gradient over the thin diffusion layer was generated towards it. Pressure gradient kept the equalization of the intra- and extracellular concentrations from progressing and the voltage gradient between them close to -81 mV (Figure 48).

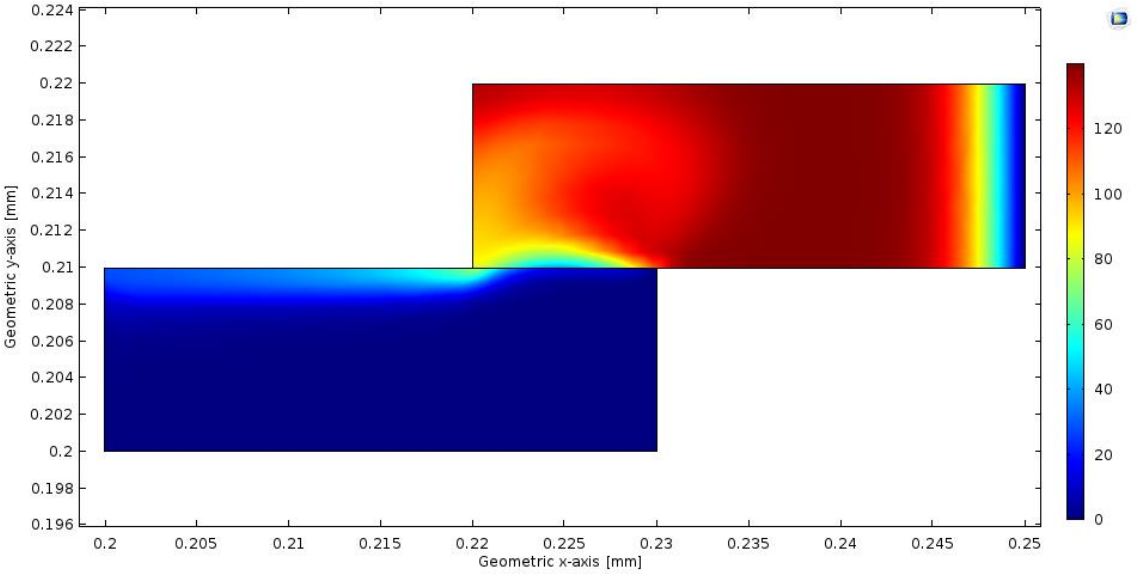

Figure 48. COMSOL D1 Ionic concentrations during the maintaining of the resting state (time 4.0 ms); concentrations are weighed with colours which are described by the legend on the right of the graph (mol/m^3)

By having the intracellular inflow take over, the depolarization effect was achieved. Highest flow velocities from the intracellular channel during the first pulse were present at the simulation time of 5.15 ms (Figure 49).

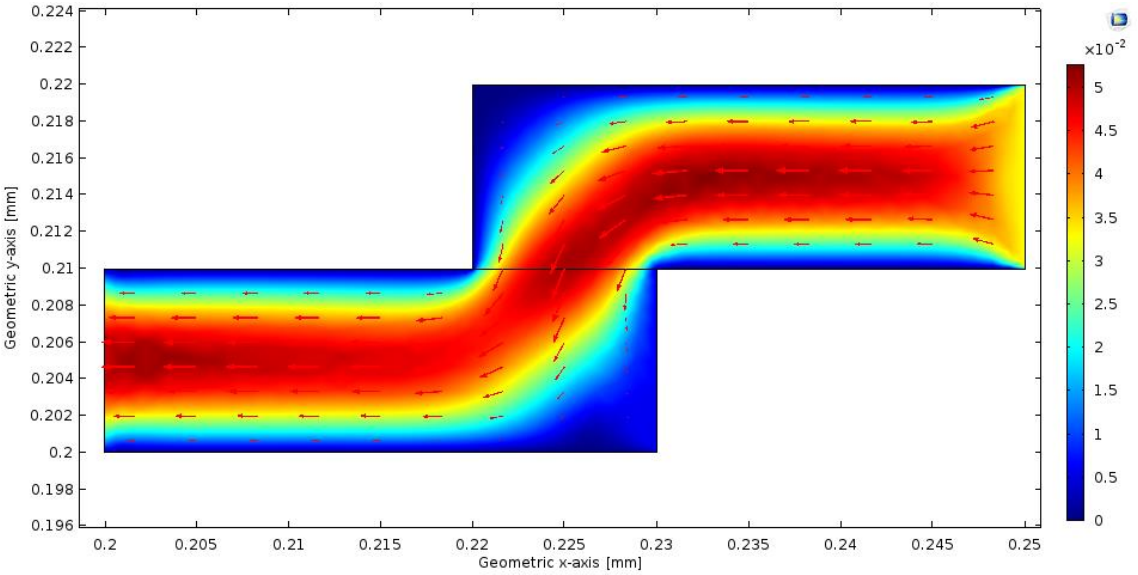

Figure 49. COMSOL D1 Flow velocities during the depolarization (time 5.15 ms); flow velocities are weighed with colours which are described by the legend on the right of the graph ($x10^{-2}$ m/s)

On Figure 49, the intracellular inflow took the shortest path, avoiding the forming pressure pockets in the two corners represented with lowest flow velocities. The regions with less flow fields inhibited the reversal of concentrations, however, this was solved by generating negative extracellular flow. Even so, the concentrations lagged, causing the highest positive gradient deviation to occur 0.72 ms after (Figure 50).

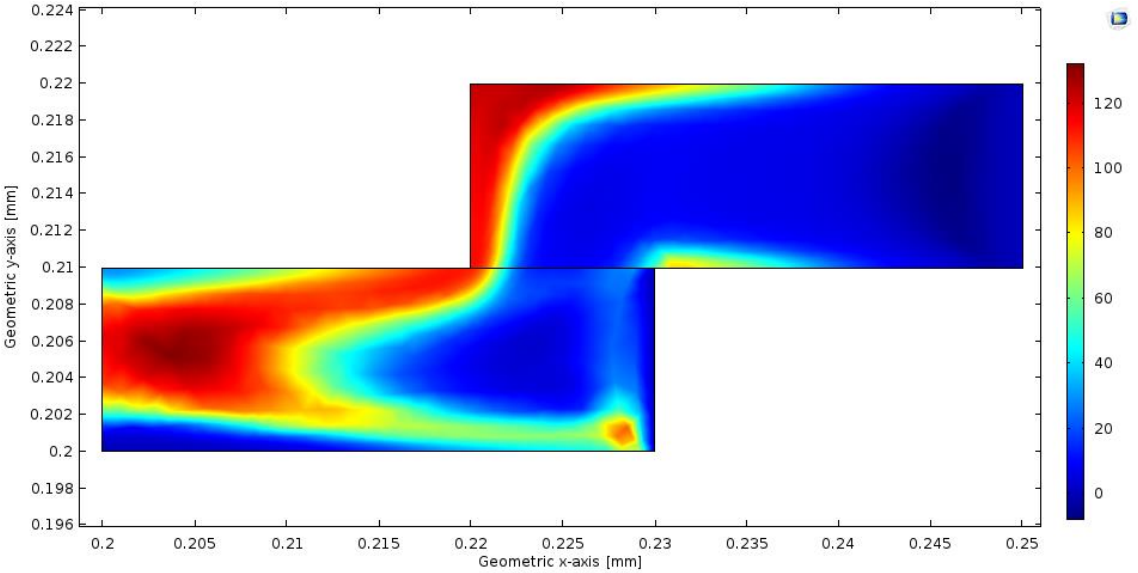

Figure 50. COMSOL D1 Concentrations at the height of depolarization (time 5.87 ms); concentrations are weighed with colours which are described by the legend on the right of the graph (mol/m3)

Repolarization of the extracellular environment was induced by returning the flow velocities of both intra- and extracellular channels to conditions presented during the resting state (Figure 47, Page 56). Lowest hyperpolarization voltage (-104.18 mV) for the first pulse was achieved by 8.23 ms of the simulation time, with the concentrations represented on Figure 51.

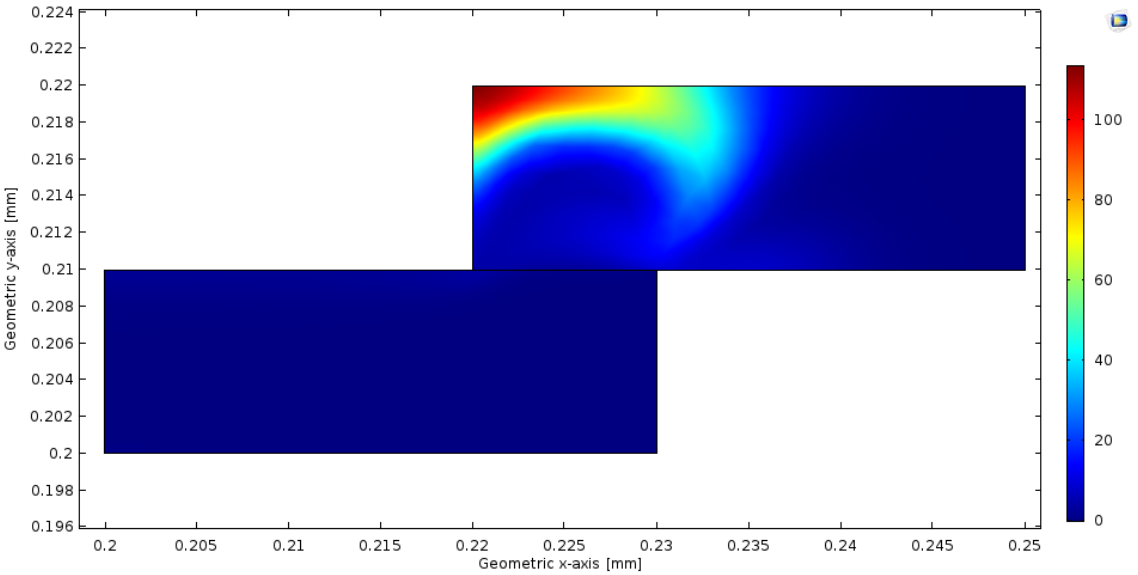

Figure 51. COMSOL D1 Concentrations during the extremity of hyperpolarization (time 8.23 ms); concentrations are weighed with colours which are described by the legend on the right of the graph (mol/m3)

In comparison to the depolarized concentrations, the concentration differences between intra- and extracellular environments during hyperpolarization show that the reproduced extracellular inflow was sufficient in returning the extracellular concentrations to normal. However, the deviations in the second generated pulse were caused by the different state the intracellular environment was left in. Longer simulation windows proved that with the used simulation parameters no more than three action potential shapes could be achieved in rapid succession, unless the full recovery of initial state was achieved.

Aside from the full AP pulse simulations, selectable voltage level simulations with design 2 version 2 in COMSOL proved the functionality of the cross-flow valve feasible, and repeatability was less of an issue. Starting from the resting state, close to -70 mV, flows in all three channels were initiated. Intra- and extracellular flow velocities given in Table 8 and Table 9 (Page 33) and cross-flow velocities given in Table 10 (Page 33) are visualised together on Figure 52 (Page 59). The voltages obtained as a result are shown in the following Figure 53.

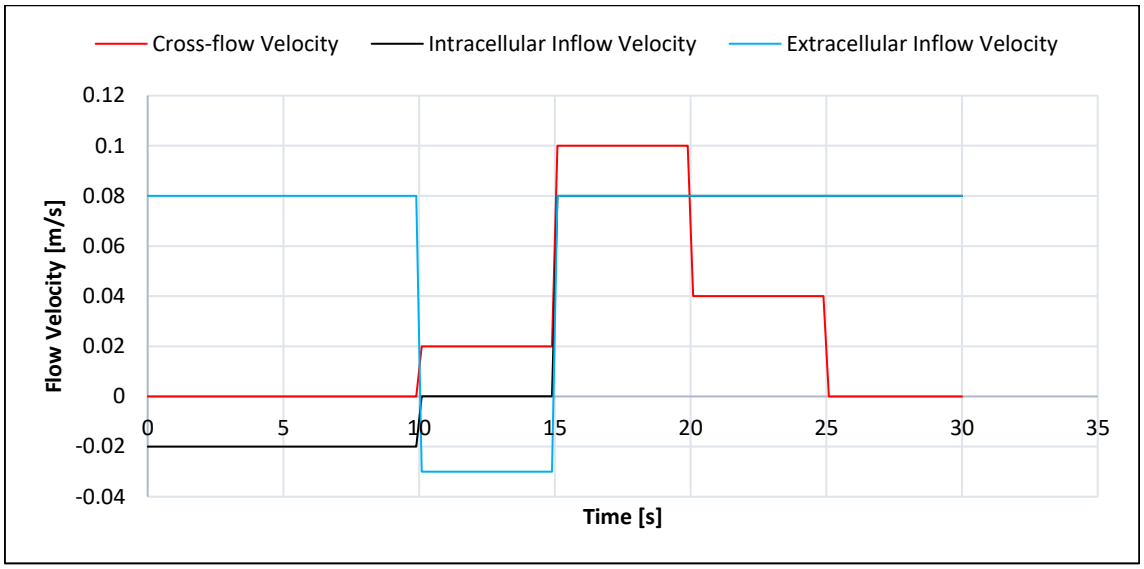

Figure 52. Graphical representation of inflow velocities in D2 controlled voltage level simulations

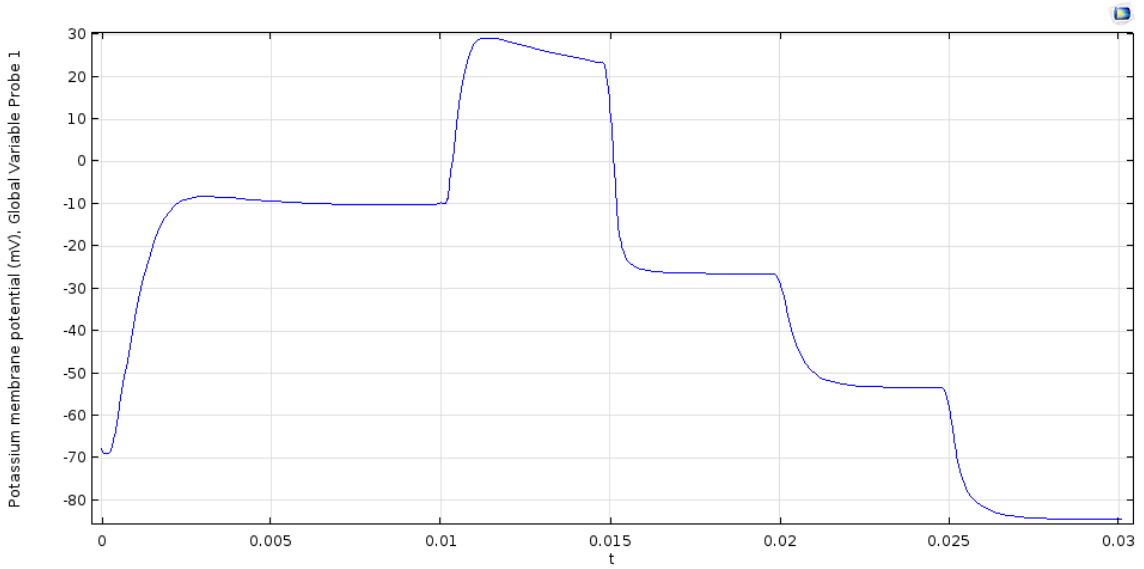

Figure 53. COMSOL simulation results; D2 version 2 controlled voltage levels with combinatory inflow velocities; highest voltage achieved at 29.214 mV; lowest voltage reached at -84.583 mV

Five controlled voltage levels are shown in 30 ms of simulation time (Figure 53). The most positive voltage level of a little over 29 mV was achieved with the help of the cross-flow concentration pulled into the extracellular environment. Holding constant positive voltages proved more difficult, negative voltage levels on the other hand, were very stable. This was mainly due to the concentration of the cross-flow valve being equal with the intracellular inflow concentration, the thin diffusion layer thickness only 1 µm and three equally non-resistive channel outlets. Close example can be seen between 15 and 20 ms of simulation time, when the cross-flow at the velocity of 0.1 m/s, dropped the voltage close to -25 mV and not 0 mV. Even though the cross-flow passes through all

three channels, due to its concentration being equal to the intracellular concentration of 140 mmol, the voltages would not equalise unless the extracellular inflow were zero or negative during that time. By reducing the cross-flow velocity step by step, normal diffusion process could gradually resume. Regarding repeatability, by using concentration levels which were close to the initial values, the initial conditions were easily resettable. In conclusion, successful AP-like signals were achieved with D1 with a negative side effect of difficult repeatability, stable controlled voltage levels successfully achieved with D2 with the side effect of more unstable positive voltages. Both simulation results proved feasibility to continue with prototyping and real-world experiments.

4.2 Experimental Analysis

All CAD model iterations were fabricated with 3D printing. During the assembly of the first printed iterations, most chips failed at the fluid tests due to mismatching of the channel boundaries or insufficient use of sealant. This was mainly due to the resin used being opaque, causing the conditions between the chips to become indeterminable. This was a serious issue for the assembly and iteration analysis. To learn about the internal conditions of both failed and usable chips, disassembly became the only option. In addition, because the top and bottom chips were glued together, disassembly was also destructive. By separating the chips, it was discovered that some failures occurred from the shifting of the membrane (specific issue for D2 v.1) and most others by the presence of NaCl residue or excessive glue on the membrane, reducing the diffusible surface area. On the other hand, successful assemblies produced varying results which were not comparable to the simulations graphs. Both manual and automated control of flow changes gave relevant visible signals on the timescale of seconds. Fastest increases of voltage, in tests with D1, were measured close to 68.8 mV/s. Acceptable measurement results were obtained only using LiBr because all measurements with NaCl solutions remained inconclusive – no characteristical signals were obtained. In addition, test setups and measurements made with D2 microfluidic chips, did not produce successfully controllable signals with any of its single Nafion sheet iterations. Leading the following measurement descriptions to centre around design 1. Throughout the manual testing with design 1, the average general settling voltage or resting state voltage was measured close to –105 mV. Measurements were started with several attempts for creating AP-like signals (Figure 54, Page 61).

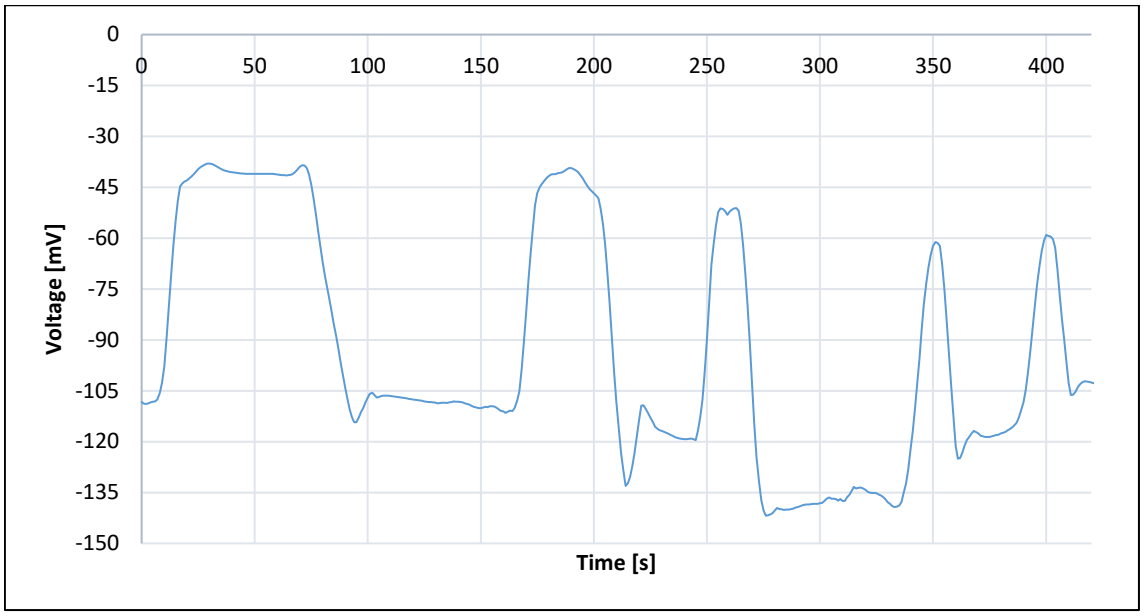

Figure 54. Manual manipulation of different LiBr concentration flows in the design 1 rev. H microfluidic chip; AP-like signals were intended; voltages shown between -141.815 and -26.795 mV

On Figure 54, five action potential-like signal shapes with varying widths can be seen. Hyperpolarization effects can also be noticed after every pulse. Varying settling voltage levels are an indication to the use of nonuniform flow velocities. The largest voltage change measured was 93.4 mV. Besides aiming to form AP-like shapes, further test in attempts in creating a variety of stable voltage levels was made (Figure 55)

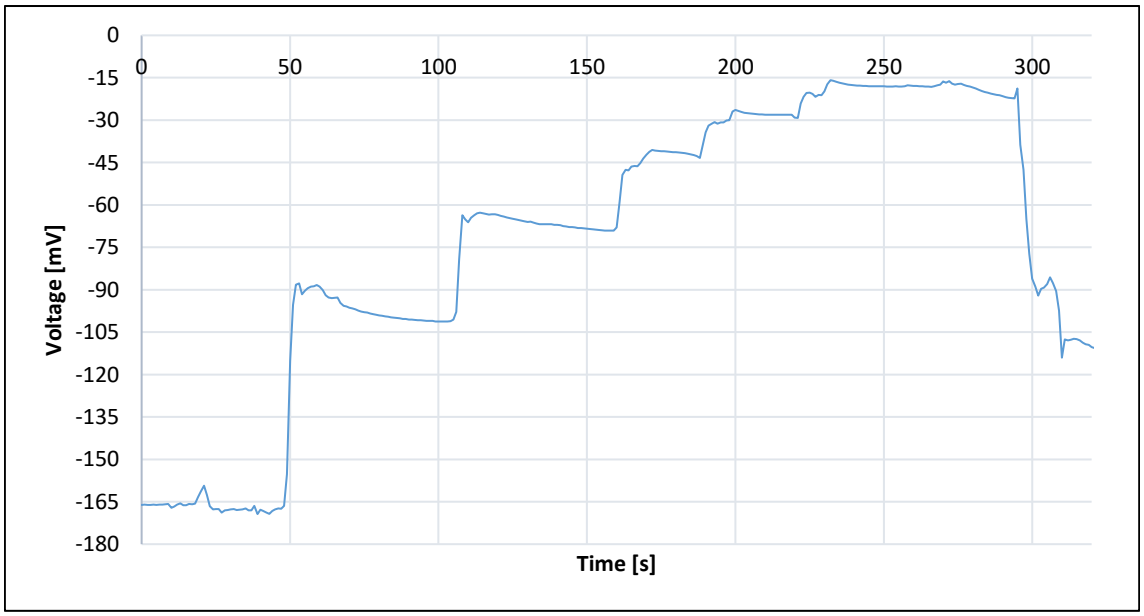

Figure 55. Manual manipulation of different LiBr concentration flows in the design 1 rev. H microfluidic chip; stable voltage levels were intended; voltages shown between -169.344 and -15.4695 mV

To further analyse the design, tests such as testing the chip's durability and recoverability against rapid switching of flow velocities between the inflow channels (Figure 56) and reaching to positive depolarization voltage levels (Figure 57) were conducted.

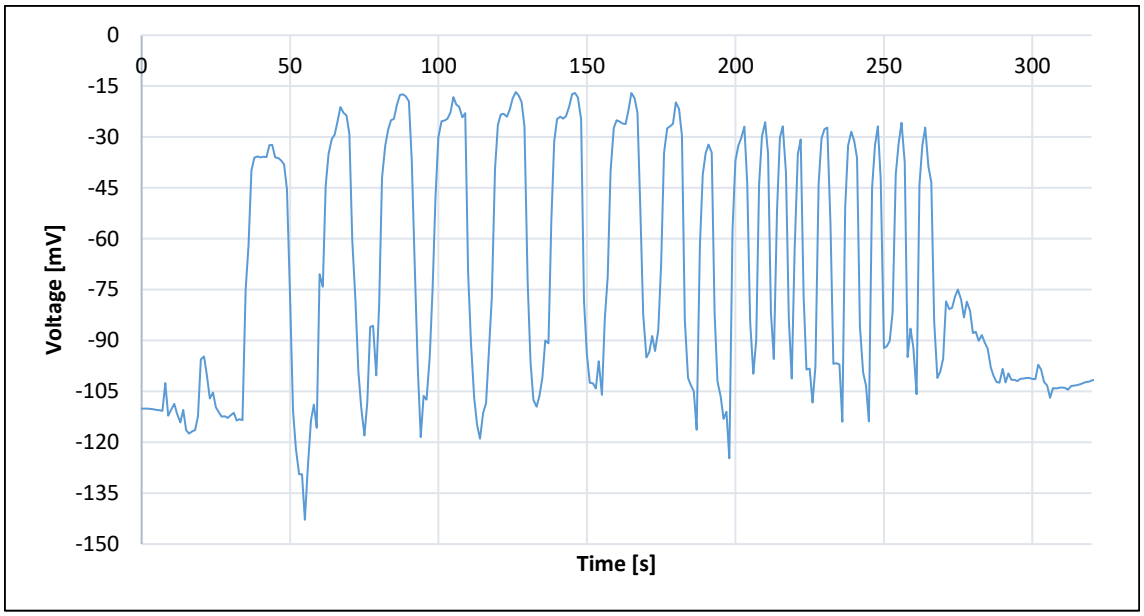

Figure 56. Manual manipulation of different LiBr concentration flows in the design 1 rev. H microfluidic chip; rapid switching signals were intended; voltages shown between -142.841 and -16.7455 mV

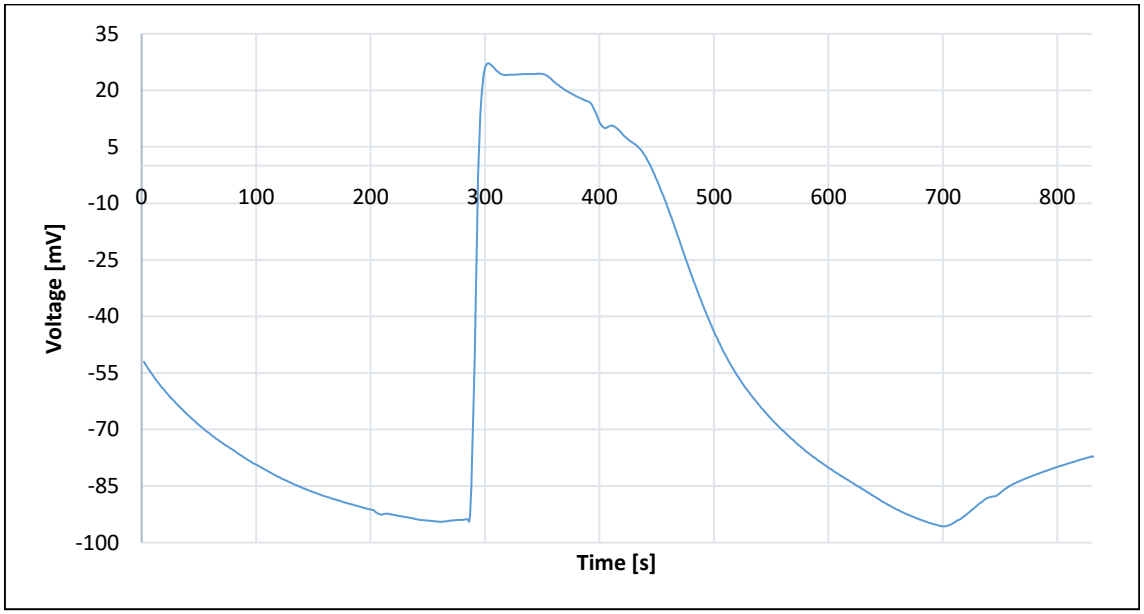

Figure 57. Manual manipulation of different LiBr concentration flows in the design 1 rev. H microfluidic chip; positive voltage levels were intended; voltages shown between -95.6909 and 27.1883 mV

To reach positive voltages, only an increase in flow velocity was required. However, as can be seen from the timeline of Figure 57, the forced repolarization process duration was

spread over several minutes. The cause of this could be explained by the occurrence of breakage or severe bowing of the Nafion XL membrane. In which case a large concentration leakage would be induced to counteract the flushing of the extracellular channel. Support for this assumption was taken from the shape of the signal after releasing the pressure from the syringes.

Producing positive voltages with automated flow controls was equally as difficult. Between several tries with the syringe pumps to achieve AP-like shapes, a single clean demonstrable pulse was obtained (Figure 58).

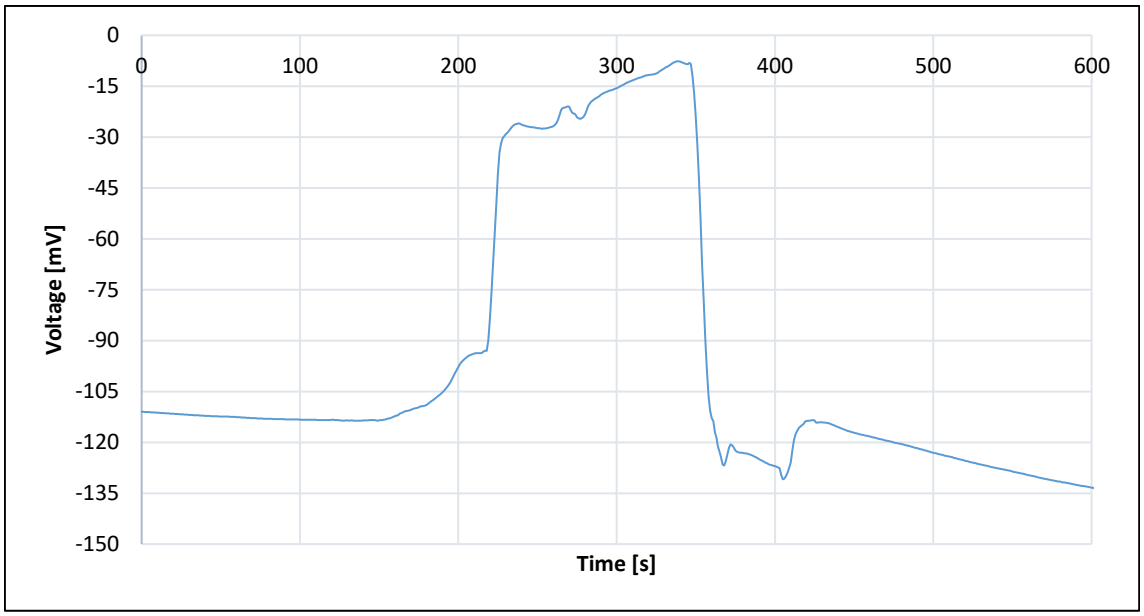

Figure 58. Automated control over different LiBr concentration flows in the design 1 rev. H microfluidic chip; AP-like signal demonstration; voltages shown between -138.849 and -7.67794 mV

In addition to not being able to obtain positive voltage levels with the netPumps, the controls available and communication method through SpinStudio Flow Software proved to be the limiting factors. The adjustability of flow speeds was not as accurate as needed and the claimed switching speeds of 10 ms were not seen with netPumps, but the several hundred millisecond delays within the local network communication media instead.

4.3 Comparison to Hodgkin-Huxley Model

By devising different designs for proving the concept of an artificial neuron in a microfluidic chip, a lot of insight was gained through the processes and results. However, most notable are the simulated action potentials with the first design. HHsim Hodgkin-

Huxley Simulator with initial settings (Figure 7, Page 20) was used to generate reference action potential data to compare with the design 1 action potentials (Figure 45, Page 55).

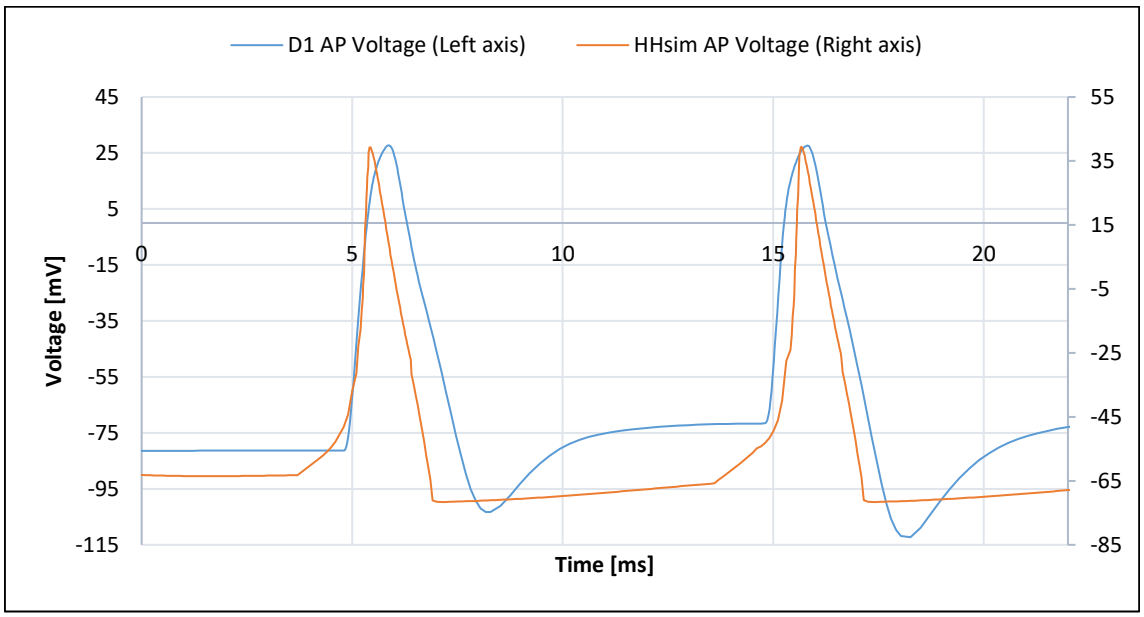

Figure 59. HHsim and COMSOL D1 action potential signal comparison

On Figure 59 with two vertical axes, the AP voltage signals have been vertically shifted into positions to provide better comparability. The average voltage difference between both AP minimums is ~15 mV and the average pulse duration is close to 0.5 ms longer for the D1 COMSOL simulations. Regarding the comparison of experimental results to the model, not enough data was obtained.

5 Summary

This work aimed to replicate the action potential formation functionality of a neuron through the use of biomimetics and microfluidics. By using the available knowledge about the subject's fundamentals, the targeted action potential was segmented into its characteristic states and explained through both its natural and artificial values. While diving into the artificial side, use cases with similar methodologies, designs and simulations were reviewed. By using previous knowledge, optimisations and guidelines were evaluated. The work progressed deeper into the devised designs and selectable options for their realisation. Parameters, shapes and functionalities of two different

COMSOL designs and their FEA simulations were given. Design 1 (flow pressure control) and design 2 (cross-flow valve) presented in COMSOL were theoretical and too simplistic to enable direct crossover into real-world microfluidic chips. In consequence, scaled up CAD models were made by using critical features from COMSOL designs and making them feasible for prototyping. For prototyping, different microfluidic actuation and fabrication methods were evaluated, from which the suitable selections helped to narrow down the structural materials. Prototypes were made from two 3D printed, opaque layers. Complementary layers were then glued together using off-the-shelf adhesive for sealant and a Nafion XL membrane positioned at respective channel interfaces, creating an artificial neuron concept in a microfluidic chip. First test on assembled prototypes included tests for membrane failures and channel leakages. However, before functionality tests followed, the experimental setup was laid out. Several system concepts were proposed which included both manual and automated pilots. The concepts were used as guidelines to explain the functionalities and roles of its components such as the desktop multimeter, syringes, netPump syringe pumps and the connective PTFE tubing. The experimental setup was concluded with the preparation of intracellular (140 mmol) and extracellular (5 mmol) ionic solutions with both NaCl and LiBr salts.

The simulated results of design 1 were successful in generating voltage signals that resembled action potentials closely. In addition to exhibiting millisecond scale durations, all biological action potential characteristics were obtained, including the resting state, depolarization, repolarization and even the hyperpolarization effect during the refractory period which in average reached 35 mV below the resting state. This proved the flow pressure control concept viable, however, it was found that the used simulation conditions caused limitations for repeatability. In simulations with design 2, the results were equally promising. The control over several stable voltage levels was demonstrated. The extended positive voltage range of cross-flow valve solution could prove a promising alternative to the Quake valve example [6]. However, similarly to the design 1, there are suggestive signs for optimization.

In contrast to the simulations, not enough experimental data was collected. The experiments with design 2 CAD models did not reach maturity due to large leakages and poor membrane position preservation discovered during or shortly after the assembly. All tests with NaCl gave insufficient results and false readings. After the destructive disassembly of the chips used in tests with NaCl, the Nafion membrane was revealed to

be covered by a layer of undissolved NaCl which was caused by the poor solubility of NaCl at room temperatures. Tests with LiBr solutions showed results which proved the functionality of design 1, however, all results were measured in a timescale of seconds. Results showed that repeatability, positive voltage, level control and the replication of hyperpolarization effects were possible.

By having obtained action potential shapes in millisecond timescales only in simulations, left the experimental results aside from further demonstrations. COMSOL simulations provided exemplary data which could be directly compared with the broadly acknowledged Hodgkin-Huxley model. The signals were showed close resemblance and a few noticeable differences. The COMSOL generated action potentials had a general bias difference of about -15 mV and a 0.5 ms repolarization delay. In comparison to a purely mathematical model, by having reached to AP signals through FEA, the findings can provide a solid foundation for further development in microfluidics.

This thesis is a milestone in a longer development process. Much of the work that needs to be done includes the creation of designs with more repeatable results, smaller physical and signal time scales, a reliable assembly and verification process. Additionally, a self-contained microfluidic artificial neuron ought to include all its presently external actuators and supplies. Beyond the development of the designs and processes, a microfluidic artificial neuron could be integrated into medical research laboratories, smart surfaces, neural networks and neurological devices capable of direct brain interfacing. The stable progress made in micro- and the coming nanofluidics looks promising for an artificial neuron to find its way forward.

References

[1] S. Herculano-Houzel, “The human brain in numbers: a linearly scaled-up primate brain.,” *Front. Hum. Neurosci.*, vol. 3, p. 31, 2009.

[2] A. Wimo *et al.*, “The worldwide costs of dementia 2015 and comparisons with 2010.,” *Alzheimers. Dement.*, vol. 13, no. 1, pp. 1–7, Jan. 2017.

[3] A. Martin Prince *et al.*, “World Alzheimer Report 2015 The Global Impact of Dementia An Analysis of prevalence, Incidence, Cost And Trends,” 2015.

[4] R. A. Freitas, *Nanomedicine, Vol. I: Basic Capabilities*. Landes Bioscience, 1999.

[5] “IBM Shows The World How To Build A Super Dense 5-Nanometer Chip.” [Online]. Available: https://www.forbes.com/sites/aarontilley/2017/06/05/ibm-5nm-chips/#773641623c56. [Accessed: 11-May-2018].

[6] T. Levi and T. Fujii, “Microfluidic Neurons, a New Way in Neuromorphic Engineering?,” *Micromachines*, vol. 7, no. 8, p. 146, Aug. 2016.

[7] E. du Bois-Reymond, “Vorläufiger Abriss einer Untersuchung über den sogenannten Froschstrom und über die elektromotorischen Fische,” *Ann. Phys.*, vol. 134, no. 1, pp. 1–30, 1843.

[8] C. J. Schwiening, “A brief historical perspective: Hodgkin and Huxley.,” *J. Physiol.*, vol. 590, no. 11, pp. 2571–5, Jun. 2012.

[9] A. L. Hodgkin and A. F. Huxley, “Currents carried by sodium and potassium ions through the membrane of the giant axon of *Loligo*,” *J. Physiol.*, vol. 116, no. 4, pp. 449–472, Apr. 1952.

[10] A. L. HODGKIN and A. F. HUXLEY, “A quantitative description of membrane current and its application to conduction and excitation in nerve.,” *J. Physiol.*, vol. 117, no. 4, pp. 500–44, Aug. 1952.

[11] D. T. Simon *et al.*, “An organic electronic biomimetic neuron enables auto-regulated neuromodulation,” *Biosens. Bioelectron.*, vol. 71, pp. 359–364, Sep.

2015.

[12] T. A. Zawodzinski, M. Neeman, L. O. Sillerud, and S. Gottesfeld, "Determination of water diffusion coefficients in perfluorosulfonate ionomeric membranes," *J. Phys. Chem.*, vol. 95, no. 15, pp. 6040–6044, Jul. 1991.

[13] J. Ni, B. Wang, S. Chang, and Q. Lin, "An integrated planar magnetic micropump," *Microelectron. Eng.*, vol. 117, pp. 35–40, Apr. 2014.

[14] "OB1 - 4 channels microfluidic flow controller - Elveflow." [Online]. Available: https://www.elveflow.com/microfluidic-flow-control-products/flow-control-system/pressure-controller/. [Accessed: 10-May-2018].

[15] S.-J. J. Lee and N. Sundararajan, *Microfabrication for microfluidics*. Artech House, 2010.

[16] Y.-J. Pan and R.-J. Yang, "A glass microfluidic chip adhesive bonding method at room temperature," *J. Micromechanics Microengineering*, vol. 16, no. 12, pp. 2666–2672, Dec. 2006.

[17] "Perfactory 4 Standard - Technical Data," 2017. [Online]. Available: https://envisiontec.com/wp-content/uploads/2016/09/2017-P4-Standard-Series.pdf. [Accessed: 05-May-2018].

[18] "LS600 | 3D Printing Materials | EnvisionTEC." [Online]. Available: https://envisiontec.com/3d-printing-materials/micro-materials/ls600/. [Accessed: 07-May-2018].

[19] G. Hernández-Flores, H. M. Poggi-Varaldo, and O. Solorza-Feria, "Comparison of alternative membranes to replace high cost Nafion ones in microbial fuel cells," *Int. J. Hydrogen Energy*, vol. 41, no. 48, pp. 23354–23362, Dec. 2016.

[20] "RS Pro Copper Sheet, 300mm x 300mm x 0.35mm." [Online]. Available: https://docs-emea.rs-online.com/webdocs/1505/0900766b81505631.pdf. [Accessed: 07-May-2018].

[21] D. Fuel Cells, "DuPont™ Nafion ® PFSA Membranes NR-211 and NR-212 Description Description."

[22] K. Kovács, “SpinSplit netPump Technical specification (Rev 1.1),” 2017. [Online]. Available: https://drive.google.com/file/d/0B0X8Bi3eUwzOTldpUVV3M1d2OFU/view. [Accessed: 06-May-2018].

[23] “Keysight Technologies 34410A and 34411A Multimeters.” [Online]. Available: https://literature.cdn.keysight.com/litweb/pdf/5989-3738EN.pdf?id=737854. [Accessed: 06-May-2018].

[24] A. Apelblat and A. Tamir, “Enthalpy of solution of lithium bromide, lithium bromide monohydrate, and lithium bromide dihydrate, in water at 298.15 K,” *J. Chem. Thermodyn.*, vol. 18, no. 3, pp. 201–212, Mar. 1986.